# Classical and quantum spin dynamics in the fcc antiferromagnet $NiS_2$ with frustration

M. Matsuura,[1,*] Y. Endoh,[1,2,†] H. Hiraka,[2] K. Yamada,[3,‡] A. S. Mishchenko,[4,5] N. Nagaosa,[6,7,8,9] and I. V. Solovyev[10,11]
[1]*Core Research for Evolutional Science and Technology, Japan Science and Technology Corporation, Kawaguchi 332-0012, Japan*
[2]*Institute for Materials Research, Tohoku University, Aoba-ku, Sendai 980-8577, Japan*
[3]*Institute of Chemical Research, Kyoto University, Gokasho, Uji, Kyoto 611-0011, Japan*
[4]*CREST, Japan Science and Technology Corporation, AIST, Tsukuba Central 4, Tsukuba 305-8562, Japan*
[5]*Russian Research Centre "Kurchatov Institute," 123182 Moscow, Russia*
[6]*Correlated Electron Research Center, AIST, Tsukuba Central 4, Tsukuba 305-8562, Japan*
[7]*Department of Applied Physics, University of Tokyo, Bunkyo-ku, Tokyo 113-8656, Japan*
[8]*ERATO Japan Science and Technology Corporation, c/o AIST, Tsukuba Central 4, Tsukuba 305-8562, Japan*
[9]*Control and Application of Nano-Structural Materials for Advanced Data Processing and Communications, CREST, Japan Science and Technology Corporation, Japan*
[10]*Institute for Solid State Physics, University of Tokyo, Kashiwanoha 5-1-5, Kashiwa 277-8531, Japan*
[11]*PRESTO, Japan Science and Technology Corporation, Japan*
(Received 16 July 2002; revised manuscript received 15 January 2003; published 9 September 2003)

The unusual coexistence of two antiferromagnetic (AF) long-range orderings (LRO) in single-crystal $NiS_2$ is investigated through measurements of inelastic neutron scattering, specific heat, uniform magnetic susceptibility, and resistivity. Neutron scattering intensity reveals a honeycomb pattern of the intensity distribution in reciprocal lattice space (continuous-line structure along the Brillouin zone boundaries) in the extended critical temperature region ($T_{N1}=39.3$ K$<T<150$ K) providing direct evidence for nearly frustrated antiferromagnetism on the face centered cubic (fcc) lattice. The observed geometrical pattern of the critical scattering makes it possible to determine the exchange coupling constants between the first, second, and third nearest neighbors, which are found to be consistent with LDA$+U$ band calculation. The system is found to be located very close to the phase boundary between the type-I AF state with $\mathbf{Q}_{\mathrm{AF}}=(1,0,0)$, and the type-II AF state with $\mathbf{Q}_{\mathrm{AF}}=(1/2,1/2,1/2)$. Theoretical analysis based on the Onsager reaction field reproduces the various features in experiments at a semiquantitative level. The type-I AF order appears the highest Néel temperature $T_{N1}=39.3$ K, while at $T_{N2}=30.6$ K, the type-I and type-II AF LRO coexist via a first-order phase transition accompanied by a small but finite lattice distortion. This coexistence is explained in terms of coupling between the spin and lattice in the nearly degenerate case, although the type-I and type-II AF LRO become mutually incompatible in the fcc symmetry at higher temperatures. The AF LRO and lattice distortion lift the degeneracy and the accumulation of spectral weight at low energy, recovering the quantum nature (spin-wave excitation) of the spin fluctuation.

DOI: 10.1103/PhysRevB.68.094409 PACS number(s): 75.25.+z, 75.40.Gb, 75.50.Ee

## I. INTRODUCTION

Nearest-neighbor antiferromagnetic (AF) interaction acting on a spin loop that includes an odd number of spins gives rise to an inherent geometrical frustration effect in magnetic systems. This frustration causes high degeneracy of ground states, resulting in a range of intriguing phenomena that have attracted intense interest for many years.[1] One of the central issues in the physics of geometrically frustrated magnets is the possible quantum spin liquid state, in which many spin configurations become degenerate due to frustration, suppressing magnetic long range ordering (LRO) down to the lowest temperature. It is thought that this degeneracy may be lifted by quantum fluctuation, giving rise to a quantum liquid state without any breaking of symmetry. Studies of the momentum and energy dependence of the spin fluctuation spectrum are indispensable for examining this phenomenon, and can be best achieved through neutron scattering experiments. However, very few such studies have been conducted, largely due to limitations in the production of sufficiently large single crystals for analysis. In the present study, the authors conducted a detailed and comprehensive analysis of $NiS_2$ in terms of elastic and inelastic neutron scattering, as well as specific heat and resistivity measurements. The results were expected to provide detailed information on the quantum/classical dynamics of the spin system in both momentum and energy space, and to shed light on the effects of frustration.

Previous investigations have revealed a number of frustrated systems; *kagomé* lattices[2,3] in two-dimensional (2D) systems and pyrochlores,[4–7] and spinel lattices[8,9] in three-dimensional (3D) systems. Degeneracy of different magnetic states leads to unusual thermodynamic properties and lattice distortion.[10–12] The face-centered cubic (fcc) lattice of interest in the present study is the simplest structure of the known frustrated 3D systems containing tetrahedra spin loop. The Fourier transformation of the exchange interaction $\mathcal{L}(\mathbf{Q})$ (as described later in the text) for antiferromagnetism on the fcc lattice in terms of solely nearest-neighbor interaction has a maximum along a one-dimensional line in momentum space, such as $\mathbf{Q}=(\pm\pi,Q_y,0)$. In this respect, antiferromagnetism on the fcc lattice has a common feature with antiferromagnetism in 2D systems, and as such can be expected to exhibit suppressed AF LRO down to low temperatures and an ex-

 

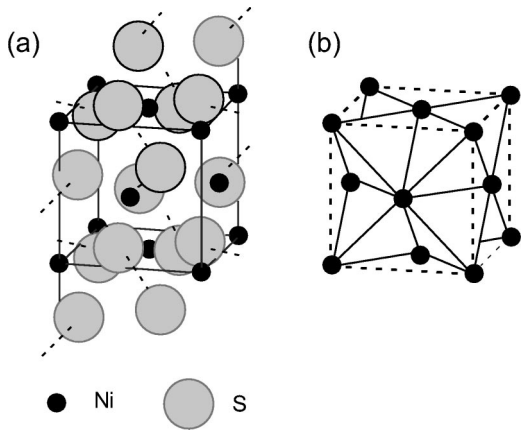


FIG. 1. (a) Pyrite structure of $NiS_2$. Ni atoms and arrays of sulfur atoms form a NaCl structure. The sulfur atoms (solid outline) form octahedral surrounding one Ni atom. (b) Edge-sharing tetrahedra in the fcc lattice.

tended critical region with the possibility of a spin liquid state. However, antiferromagnets on fcc lattices often exhibit stable AF LRO [type-I, $\mathbf{Q}_{\mathrm{AF}}=(1,0,0)$; type-II, $\mathbf{Q}_{\mathrm{AF}}=(1/2,1/2,1/2)$; and type-III, $\mathbf{Q}_{\mathrm{AF}}=(1,1/2,0)$]. These fcc AF LRO are well explained by a classical Heisenberg model with several next-to-nearest neighbor exchange interactions or magnetocrystalline anisotropy.

Despite detailed knowledge of some fcc antiferromagnets, there are a number for which the current understanding is far from complete. Examples of these unusual compounds include MnO (NaCl structure),[13] $MnS_2$ (pyrite),[14] and $(NH_4)_2IrCl_6$ (fcc salt),[15] which exhibit magnetic ordering by a first-order transition accompanied by structural phase transition. The Néel temperature ($T_N$) for these compounds is $5\sim12$ times smaller than the Curie-Weiss temperature, suggesting suppression of AF LRO.[16] Two other pyrite materials that exhibit fcc antiferromagnetism, $MnSe_2$ and $NiS_2$, are characterized by the unusual coexistence of two AF LRO; types I and III for $MnSe_2$ (Ref. 17) and types I and II for $NiS_2$.[18,19] The coexistence of different AF LRO is impossible in these crystal structures if only two-spin interactions are taken into account. Although four-spin exchange interactions are expected to be important in these systems,[20,21] such interactions will be critical for the coexistence of LRO only if the possibility of structural distortion is disregarded.

The present study focuses on $NiS_2$, which has been investigated as a typical Mott insulator from the 1970's, exhibiting semiconducting behavior in spite of partially (half) filled bands.[22] Figure 1(a) shows the pyrite structure of $NiS_2$, in which Ni and $S_2$ form a NaCl structure. The $Ni^{2+}$ ions form a fcc lattice of edge-sharing tetrahedra [Fig. 1(b)] surrounded by octahedral $S^{1-}$ ions. This structure has more bonds to next sites than a corner-sharing tetrahedra structure, and as such has lower degeneracy of ground states. $NiS_2$ is in a low-spin state, giving rise to two $e_g$ states, i.e., spin $S=1$. Although the $e_g$ bands split into upper and lower Hubbard bands with strong Coulomb interaction, recent resonant photoemission spectroscopy measurements have revealed that the charge excitation in $NiS_2$ is in fact governed by charge transfer between the $3d$ band of the transition metal and the $2p$ band of the ligand atom.[23]

$NiS_2$ exhibits a complicated spin structure and unusual magnetic phase transitions at low temperature.[19] Type-I AF LRO is the first to appear at 39.3 K ($T_{N1}$). Using polarized neutron diffraction, Kikuchi *et al.* showed that this LRO is noncollinear.[24,25] The spin lattice of the type-I AF consists of four sublattices with a unit cell equivalent to the chemical cell, where the four spins point to $[\mu_x\ \mu_y\ \mu_z]$, $[\mu_x\ \overline{\mu_y}\ \overline{\mu_z}]$, $[\overline{\mu_x}\ \mu_y\ \overline{\mu_z}]$, and $[\overline{\mu_x}\ \overline{\mu_y}\ \mu_z]$. Above $T_{N2}$, each spin forms a constant angle of $\theta=12\pm4°$ with the symmetry axis, i.e., $\cos\theta=(\mu_x+\mu_y+\mu_z)/\sqrt{3}$.[26] At $T=30.6$ K ($T_{N2}$), type-II AF LRO arises through a first-order transition accompanied by a discontinuous increase in the type-I AF order parameter and $\theta$. Weak-ferromagnetism (WF) also occurs due to a slight canting of the spin direction towards [100]. These three orderings coexist below $T_{N2}$.[27] Although a breaking of crystal symmetry at $T_{N2}$ has been reported based on thermal expansion[28] and x-ray diffraction measurements,[29] different types of distortion were identified: tetragonal (thermal expansion) and rhombohedral (x ray). Recently, Shindou and Nagaosa proposed a mechanism of WF based on spin chirality due to the noncoplanar spin configuration, where a small lattice distortion yields orbital ferromagnetism.[30] In addition to the unusual AF LRO, anomalous behavior has also been observed in the paramagnetic phase, where the magnetic susceptibility exhibits negative curvature up to 300 K in contradiction of the Curie-Weiss law,[29,31] and the Hall effect and electrical resistivity shows metallic behavior below 150 K.[31,32]

Although a few anomalous fcc antiferromagnets have been identified, there is as yet no direct evidence of geometrical frustration in fcc antiferromagnets. Detailed study of momentum ($\mathbf{q}$) and energy ($\omega$) dependence of the generalized spin susceptibility $\chi''(\mathbf{q},\omega)$ is indispensable in the study of the spin dynamics of such systems. By fixing parameters in the theory, this method can be expected to give a realistic description of these materials. The present authors have performed inelastic neutron scattering experiments on $NiS_2$ using single crystals and observed anomalous magnetic critical scattering at the Brillouin zone boundaries of a chemical unit cell as a 3D frustrated magnet $(Y_{0.97}Sc_{0.03}Mn_2)$.[33] This observation indicates that a heuristic relationship exists between the unusual magnetism in $NiS_2$ and geometrical spin frustration. Magnetic critical scattering was observed even at up to 300 K (7.5 times $T_{N1}$) and was enhanced below 150 K, representing direct evidence of geometrical spin frustration in the fcc antiferromagnet. Detailed analysis of the observed scattering intensity in $NiS_2$ revealed that the system is very close to the phase boundary between the two types of AF LRO, which is also supported by LDA+$U$ calculations. This quasidegeneracy makes the spin fluctuation almost classical because the spectral weight is accumulated in the energy region lower than the thermal energy $k_BT$. The classical to quantum crossover is triggered by the LRO and/or the structural phase transition. This is because the spin wave dispersion is induced by the LRO, and its energy goes beyond $k_BT$. This fact contradicts the initial

expectation that frustration should *enhance* the quantum nature of spin. In fact, frustration *suppresses* the quantum nature down to lower temperatures by extending the classical critical region. This paper is structured as follows. Section II presents the details of experiments and Sec. III reports the experimental results for uniform magnetic susceptibility, resistivity, and specific heat. The neutron scattering results are given in Sec. IV, followed by a theoretical analysis in Sec. V. Section VI presents the discussions and conclusions.

## II. EXPERIMENTAL DETAILS

Single crystals of $NiS_2$ were grown by a chemical vapor transport method using $Cl_2$ and $Br_2$ gas. The detailed conditions of crystal growth are described in a previous paper.[31] The typical sizes of single crystals grown using $Br_2$ gas were larger ($\sim 0.15\ cm^3$) than those produces using $Cl_2$ gas ($\sim 0.1\ cm^3$), but the mosaicness of former was twice that of the latter. Therefore, the crystals grown using $Cl_2$ gas were employed for transport and magnetic susceptibility measurements, while both types of crystals were examined in neutron scattering measurements. All single crystals had shiny (100), (111), and (210) facets.

Neutron inelastic scattering measurements were performed on the triple-axis spectrometer TOPAN installed at the JRR-3M Reactor of the Japan Atomic Energy Research Institute. The final neutron energy was fixed at 14.7 or 30.5 meV using a pyrolytic graphite (PG) analyzer. The horizontal collimation of the neutron beam was set at 40′-30′-60′-80′ from reactor to detector. A PG filter was placed in front of the analyzer to eliminate higher-order contamination from the incident beam. To ensure a sufficiently high signal-to-noise ratio, a total of 9 single crystals ($\approx 1$ cc) were used, aligned by utilizing the shiny (100) and (111) facets. Magnetic excitations from the type-I [$\mathbf{Q}_{AF}=(100)$] and the type-II [$\mathbf{Q}_{AF}=(1/2,1/2,1/2)$] AF LRO were measured in the (*hkk*) scattering zone. The uniform magnetic susceptibility $\chi$ was measured using a standard SQUID magnetometer for $T \leqslant 300$ K and a vibrating sample magnetometer for $300 \leqslant T \leqslant 700$ K. The electrical resistivity $\rho$ was measured by a standard four-probe method between 4.2 and 300 K, and the specific heat at constant pressure was taken by a heat-pulse method in an adiabatic cell from 1.5 to 50 K, and by an ac calorimetry above 15 K.

## III. MAGNETIC AND TRANSPORT PROPERTIES

The characteristic features of magnetic and transport properties for frustrated magnets were clearly observed in this experiment. Figure 2(a) shows the temperature dependence of the inverse magnetic susceptibility $\chi^{-1}$ in an applied magnetic field of $H=1$ T along the [100] direction. Previous work reported unusual $\chi(T)$ behavior that does not obey the Curie-Weiss law below 300 K.[29,34,35] From measurements of $\chi$ at temperatures above 300 K, $\chi(T)$ was found in present study to begin to deviate from the Curie-Weiss law at around 350 K. The Curie-Weiss temperature ($\Theta_{CW}$) calculated from $\chi^{-1}(T)$ above 400 K is $-1250 \pm 2$ K, which indicates strong suppression of the AF LRO

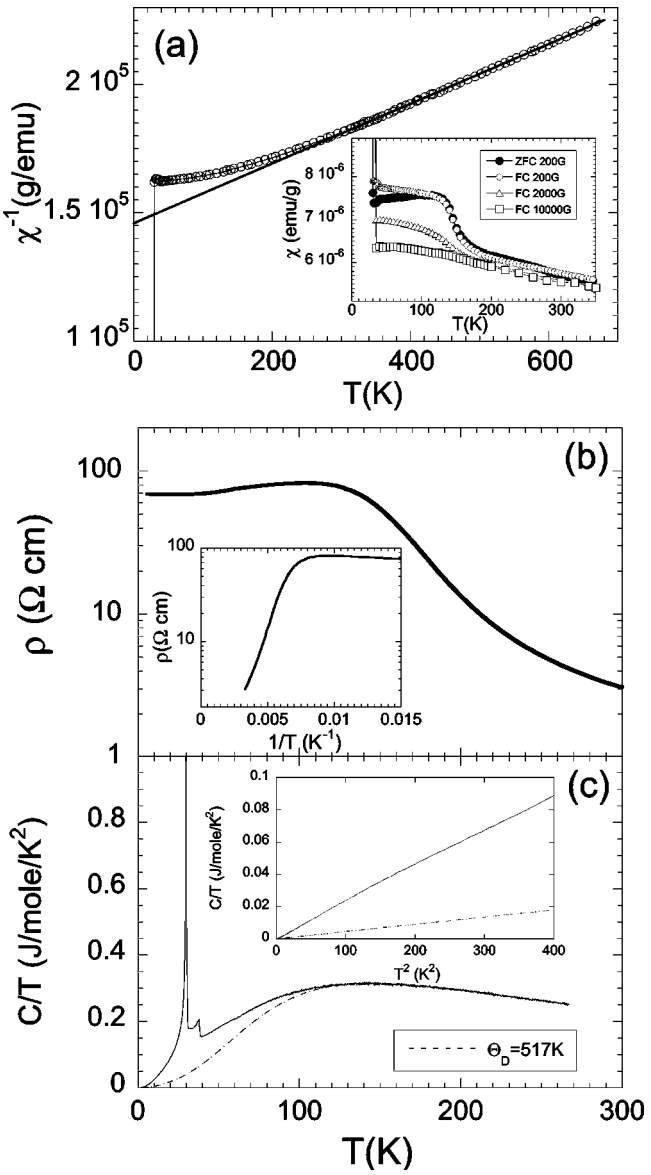


FIG. 2. (a) Temperature dependence of inverse magnetic susceptibility $\chi^{-1}$ under a magnetic field applied along the [100] direction. The straight line shows the fit to the Curie-Weiss law. The inset shows the temperature dependence of $\chi$ for zero-field cooling (ZFC) and field cooling (FC) under several magnetic fields. (b) Electrical resistivity $\rho$ on the (100) plane as a function of $T$ and $T^{-1}$ (inset). The value of $\rho$ deviates from semiconducting behavior below 150 K and exhibits metallic behavior at low temperature. (c) Specific heat divided by temperature ($C/T$) vs temperature. The dotted line shows the lattice contribution of $\Theta_D=517$ K. The inset shows $C/T$ as a function of $T^2$.

($-\Theta_{CW}/T_{N1} \approx 30$). An effective moment of $2.90 \pm 0.01\ \mu_B$ is estimated from the slope of the Curie-Weiss curve, which agrees well with $g\sqrt{S(S+1)}=2.83$ for $S=1$ and $g=2$. Using these values with the mean-field theory, taking into account only nearest-neighbor exchange interactions $J=3k_B\Theta_{CW}/zS(S+1)$ is calculated to be $13.5 \pm 0.1$ meV. Here, $z$ is the number of nearest-neighboring atoms, and is taken as 12 in this case.

In a weak magnetic fields, spin-glass behavior was ob-

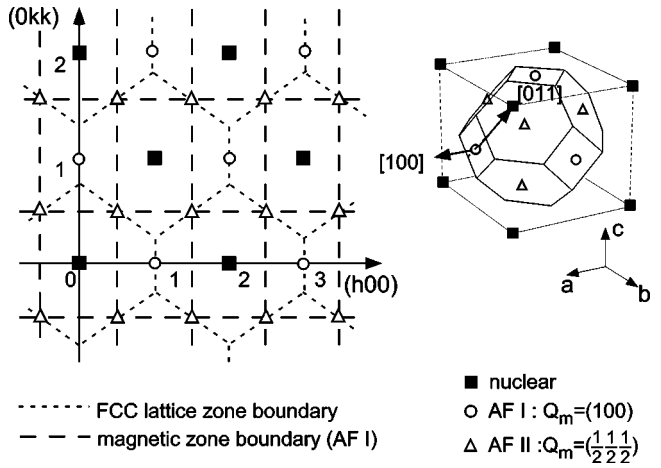


FIG. 3. Schematic diagram of (*hkk*) scattering plane and Brillouin zone of the fcc unit cell. The type-I and type-II AF Bragg points are located at the center of rectangular and hexagonal planes forming the fcc Brillouin zone boundaries, respectively.

served, as shown in the inset of Fig. 2(a). Below 150 K, there is a clear difference between field-cooled (FC; open circles) and zero field-cooled (ZFC; closed circles) $\chi$ in a 0.02 T magnetic field. The enhanced $\chi$ below 150 K decreases with increasing field strength $H$, and almost disappears at $H=1$ T. The magnetization curve $M(H)$ exhibits an almost linear field-dependence, except for a slight hump at 0.1 T below 150 K. The enhancement is proportional to the ratio of surface area to volume, indicating that the short-range ferromagnetic ordering can be pinned by crystal defects on the surface.

Anomalous behavior below 150 K was also observed in the transport properties. Figure 2(b) shows the temperature dependence of electrical resistivity $\rho$ on the (100) plane. At high temperatures, $\rho$ increases exponentially with decreasing temperature. The activation energy estimated from the slope of $\ln\rho$ vs $T^{-1}$ [inset of Fig. 2(b)] is 80 meV, which is consistent with previous reports.[36] The slope $d\rho/dT$ decreases rapidly to become negative at around 150 K, and $\rho$ itself is characteristically metallic below 150 K, also as determined in a previous study.[32]

Figure 2(c) shows the temperature dependence of specific heat $C$. The specific heat exhibits two successive divergences at low temperatures, attributed to magnetic phase transitions at $T_{N1}$ (39 K) and $T_{N2}$ (31 K). The inset of Fig. 2(c) shows the $T^2$ dependence of $C/T$. At low temperatures, a linear contribution $\gamma T$ to the specific heat is zero. Therefore, the total specific heat $C$ consists of magnetic ($C_{\rm mag}$) and phonon ($C_{\rm phonon}$) contributions. The molar lattice specific heat under constant pressure ($C_{\rm phonon}$) is estimated to be the same as in the previous report.[37] The Debye temperature is $\Theta_D=517\pm2$ K, as determined from fitting at high temperatures [dotted line in Fig. 2(c)]. The difference between $C$ and $C_{\rm phonon}$ becomes appreciable below 150 K, seen in figure. Below $T_{N2}$, $C_{\rm mag}$ is proportional to $T^3$, which is expected for the magnetic contribution of spin waves in a 3D antiferromagnet. The spin wave contribution is given as $C_{\rm mag}=3.17\times10^{24}\times k_B(k_BT/A)^3$ [J/mole K], where $A$ is the spin wave stiffness constant for antiferromagnet $\hbar\omega=A|\mathbf{q}|$. From the coefficient of the $T^3$ term in $C_{\rm mag}$, $A$ is calculated to be $11.5\pm0.1$ meV Å by using the above formula.

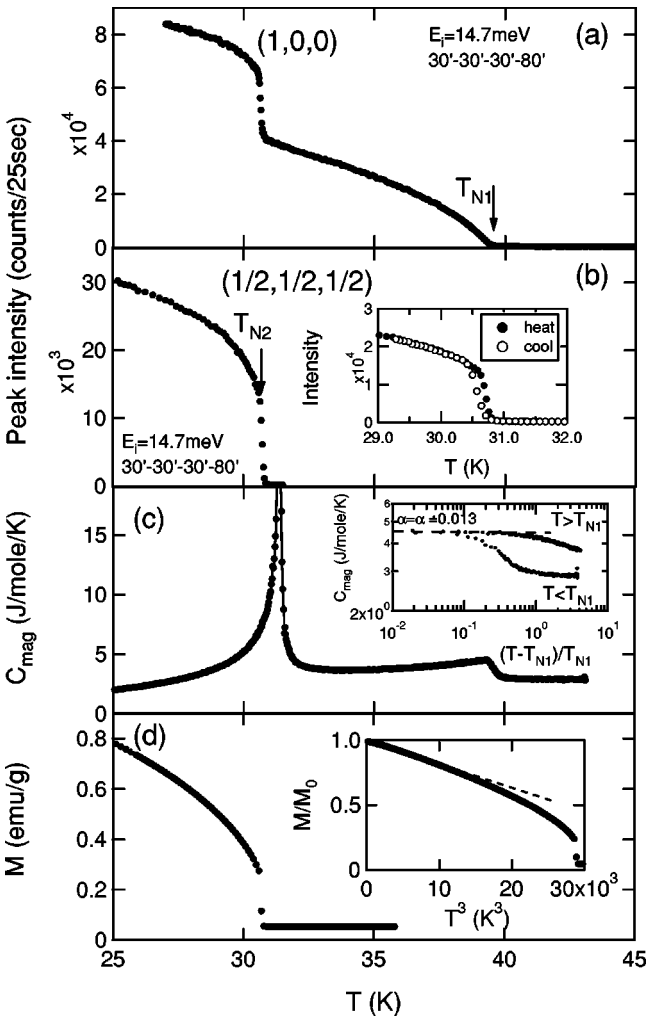


FIG. 4. Temperature dependence of the peak intensity of (a) the type-I AF Bragg (100) peak and (b) the type-II AF Bragg (1/2, 1/2,1/2) peak. The inset in (b) shows data for heating (closed circles) and cooling (open circles). (c) Magnetic contribution of specific heat $C_{\rm mag}$ as a function of $T$ and normalized temperature. Dotted line in the inset represents a fit with a critical exponent of $\alpha=\alpha'=0.013$. (d) Thermal variation of magnetization under a magnetic field of 1 T along the [100] direction. Inset shows magnetization normalized to that at $T=0$ as a function of $T^3$.

In the (*hkk*) scattering plane, the Brillouin zone boundary (ZB) of the fcc unit cell has a honeycomb structure, as shown in the left panel of Fig. 3. In reciprocal space, the fcc ZB consists of rectangular and hexagonal planes (the right panel). Note that the type-I and type-II AF Bragg points are on the fcc ZB at the center of the rectangular and hexagonal planes, respectively. Although a small distortion occurs below $T_{N2}$, this distortion is ignored and the indices within the fcc unit cell are denoted throughout the present paper. Elastic neutron scattering measurements confirmed the existence of two types of sharp Bragg reflections and two successive phase transitions. Figures 4(a) and 4(b) show the temperature

TABLE I. Three characteristic temperature regimes of magnetic excitations in $NiS_2$.

| LRO and spin wave | | (A) $T<T_{N2}$ type I +type II | (B) $T_{N2}<T<T_{N1}$ type I | (C) $T>T_{N1}$ no Bragg reflection |
|---|---|---|---|---|
| Critical scattering | $Q\sim(1,0,0)$ (type I) | Inelastic $\omega\sim 12$ meV | Inelastic $\omega\sim 12$ meV | Quasielastic ——— - - ▶ |
| | $Q\sim(\frac{1}{2},\frac{1}{2},\frac{1}{2})$ (type II) | Inelastic $\omega\sim 12$ meV | Quasielastic ——— - - - ▶ | |
| | zone boundary | none | Quasielastic ——— - - - ▶ | |

dependences of the type-I AF LRO with AF wave vector (1,0,0) and the type-II AF LRO with AF wave vector (1/2, 1/2,1/2). The type-I AF LRO appears first at $T_{N1}=39.3\pm0.1$ K via a second-order transition. The critical exponent $\beta=0.306\pm0.03$ is determined from the fitting for $I_{\text{type-I}}\propto[(T-T_N)/T_N]^{2\beta}$, where $I_{\text{type-I}}$ is the peak intensity of the type-I AF Bragg point (100). This $\beta$ value is almost consistent with theoretical value for universality classes in three-dimensional systems, such as Heisenberg (0.3645), *XY* (0.345), and Ising (0.32) models. It was confirmed that the type-II AF Bragg reflection with (1/2,1/2,1/2) arises abruptly below $T_{N2}=30.6\pm0.1$ K accompanied by enhancement of the type-I AF LRO, as previously reported.[19] The critical behavior of the phase transition at $T_{N2}$ is quite different from that at $T_{N1}$. The type-II AF order parameter exhibits a small hysteresis ($\sim$0.1 K), shown in the inset of Fig. 4(b), indicating a first-order phase transition. Below $T_{N2}$, the order parameters for type-I and type-II have the same temperature dependence, which can be approximated by $[(T_{N2}-T)/T_{N2}]^{2\beta}$ with $\beta=0.22\pm0.01$.

Although the critical behavior of the AF order parameter at $T_{N1}$ is normal, the divergence of magnetic specific heat at $T_{N1}$ is unusually small. Figure 4(c) shows the specific heat data after subtraction of the lattice contribution ($\Theta_D=517$ K). The slight difference in the transition temperature is due to imperfect temperature calibration for ac calorimetry experiments. The calculated magnetic entropy release ($S_{\text{mag}}$) for $T_{N2}<T\leqslant T_{N1}$ is 1.1 J/mole K. This $S_{\text{mag}}$ is 8 times smaller than $R\ln(2S+1)=9.1$ J/mole K for $S=1$, where $R$ is the gas constant. As seen in Fig. 2(c), the magnetic entropy is released below 150 K, reaching to 2.9 J/mole K between $T_{N1}$ and 150 K. $S_{\text{mag}}$ for $T<T_{N2}$ is estimated to be only 1.9 J/mole K, and therefore the residual magnetic contribution to entropy (3.2 J/mole K) should be released mainly at $T_{N2}$. The inset in Fig. 4(c) is a logarithmic plot of magnetic specific heat vs normalized temperature. The small divergence of $C_{\text{mag}}$ gives an anomalous critical exponent of $\alpha=\alpha'=0.013\pm0.0017$ with $C_{\text{mag}}\propto[(T-T_{N1})/T_{N1}]^{-\alpha}$ for $T>T_{N1}$ and $C_{\text{mag}}\propto[(T_{N1}-T)/T_{N1}]^{-\alpha'}$ for $T<T_{N1}$, which is much smaller than for the 3D Heisenberg model ($\alpha=\alpha'=0.115$).

WF was confirmed below $T_{N2}$, as in the previous report.[38] The WF has been shown based on the results of a polarized neutron diffraction study to be due to the cant of AF ordered spins.[25] Assuming a simple linear spin-wave dispersion at small $q$, where $q$ is wave vector from AF Bragg point, the number of magnons will be proportional to the third power of temperature for 3D antiferromagnets. A plot of normalized magnetization vs $T^3$ is shown in the inset of Fig. 4(d). At low temperatures, the decrease in magnetization from the $T=0$ value ($M_0$) follows a $T^3$ law up to $T/T_{N2}\sim0.6$; $M(T)-M_0\propto T^3$, which is attributed to magnons.

## IV. INELASTIC NEUTRON SCATTERING

It was found that spin fluctuations in $NiS_2$ can be separated into three phases; a paramagnetic phase ($T>T_{N1}$), an intermediate phase ($T_{N2}<T<T_{N1}$), and a low temperature phase ($T<T_{N2}$). Furthermore, three characteristic contributions to the scattering spectra were observed; spin-wave, in-

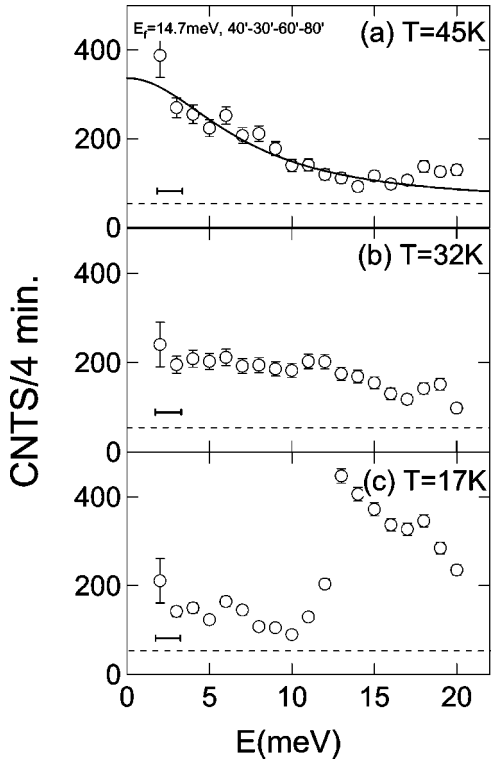


FIG. 5. Energy scan spectra at the (011) type I AF Bragg point at a temperature $T$ of (a) 17, (b) 32, (c) 45 K. The solid line in (a) is a Lorentzian fit. The horizontal bar represents the instrumental resolution width and the dashed line indicates the background.

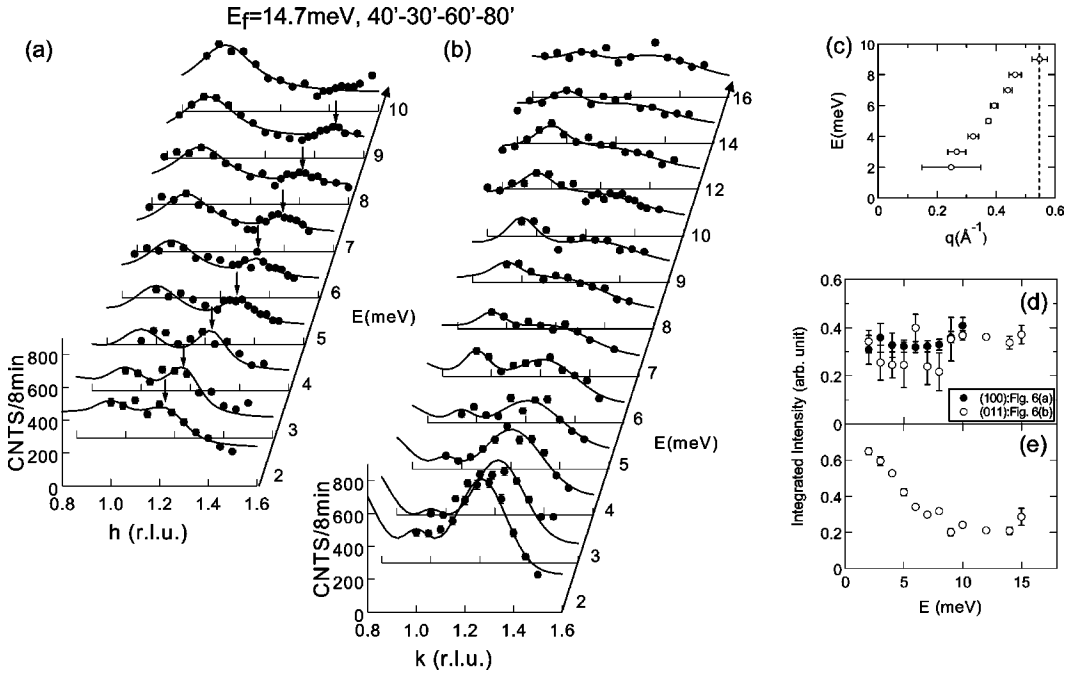


FIG. 6. **Q**-scan spectra at $T=32$ K in (a) the [100] direction from the (100) AF Bragg point with $(h00)$ and (b) the [011] direction from the (011) AF Bragg point with $(0kk)$. The fitting line is the sum of a Lorentzian function for the peak at the type-I AF Bragg point and (a) a Lorentzian function for the spin-wave signal or (b) a Gaussian function for the peak at (0,1.25,1.25), convolved with the instrumental resolution function and magnetic form factor. The arrows in (a) indicate the spin-wave peaks. (c) Spin-wave dispersion for the [100] direction. (d), (e) Energy dependence of integrated intensity of (d) the peak at the type-I AF Bragg point and (e) the peak at the crossing point of the fcc Brillouin zone boundaries.

elastic excitation above 12 meV, and critical scattering extending to the fcc ZB, as summarized in Table I. Figure 5 shows energy scans with fixed **Q** at the (011) type-I AF Bragg point for three characteristic temperatures. In the first regime, the paramagnetic phase [Fig. 5(a)], strong AF spin correlations were observed. The critical scattering can be fitted by a Lorentzian with half-width-at-half-maximum (HWHM) $\Gamma=7.0\pm0.6$ meV, as represented by a solid line in the figure. The AF short-range correlations were observed even at $T=250$ K, and were enhanced below 150 K, where the anomalies in the transport and magnetic properties appear. In the second stage, the intermediate phase $T_{N2}<T<T_{N1}$ [Fig. 5(b)], the spectrum shifts towards higher energies. Type-I AF LRO arises concomitantly with spin-wave excitations. In the low-temperature regime below $T_{N2}$ [Fig. 5(c)], the scattering at the type-I AF Bragg point becomes inelastic with a finite energy gap of 12 meV ($\approx J$), as shown in Fig. 5(c). At low energies, the spin-wave excitations were also observed near both the type-I and type-II AF Bragg points.

The magnetic excitations in the intermediate phase, where only the type-I AF LRO exists, are examined first. Figure 6 shows **Q** scans along the [100] and [011] directions around the type-I AF Bragg point at $T=32$ K, just above $T_{N2}$. In the intermediate phase, all three of above magnetic excitations are observed. The fitting line in Fig. 6(a) is the sum of two Lorentzian functions for the weak peak at the magnetic zone center and the spin-wave signal, convolved with the instrumental resolution function and magnetic form factor. Weak but clear spin-wave dispersion from the type-I AF Bragg point was observed for the [100] direction, as indicated by arrows in Fig. 6(a). A linear fit in the small $q$ region yields a spin-wave velocity of $d\omega/dq=12.6\pm0.6$ meV Å [Fig. 6(c)], where $q$ is measured from the type-I AF Bragg point, i.e., $h=1$. This spin-wave velocity is consistent with the value evaluated from the specific heat. In addition, a broad peak appears at the center of magnetic zone at all energies. The HWHM $\kappa$ of the Lorentzian peak at the magnetic zone center is about 0.11 Å$^{-1}$ in all spectra, indicating a short-range correlation extending out to the third-nearest neighbor atoms. The energy dependence of the integrated peak intensity for the peak at the magnetic zone center is shown in Fig. 6(d). The integrated intensity has a broad maximum at 12 meV, which is almost equal to the nearest-neighbor $J$, determined from the Curie-Weiss behavior of the uniform magnetic susceptibility.

Figure 6(b) shows **Q** scans along the [011] direction from the (011) type-I AF Bragg point with $(0kk)$. Although no discernable spin-wave signal was observed for the [011] direction, an intense peak appears at (0,1.25,1.25) up to 16 meV. The solid lines in the figure represent the Gaussian fit for the intense peak and the Lorentzian fit for the peak at the magnetic zone center. The position of the intense peak corresponds to the crossing point of the fcc ZB. The integrated intensity of the peak at this crossing point is shown in Fig. 6(e) as a function of excitation energy. The same energy dependence as that for diffusive scattering at the type-I AF Bragg point in the paramagnetic phase is apparent.

Figure 7 shows the **Q** dependence of critical scattering at the fcc ZB. The measurements were performed in constant-

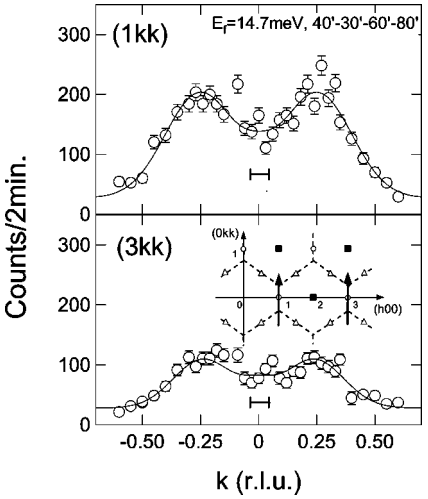


FIG. 7. **Q** dependence of critical scattering at the fcc Brillouin zone boundaries. Spectra were measured along the [011] direction around the (100) and (300) type-I AF Bragg points with an energy transfer of 2 meV at $T=32$ K. The fitting lines are the sum of a Lorentzian function for the peak at the magnetic zone center ($k=0$) and two Gaussian functions for the two strong peaks at the crossing point of the fcc Brillouin zone boundary ($k=\pm 0.25$). The horizontal bar represents the instrumental resolution width.

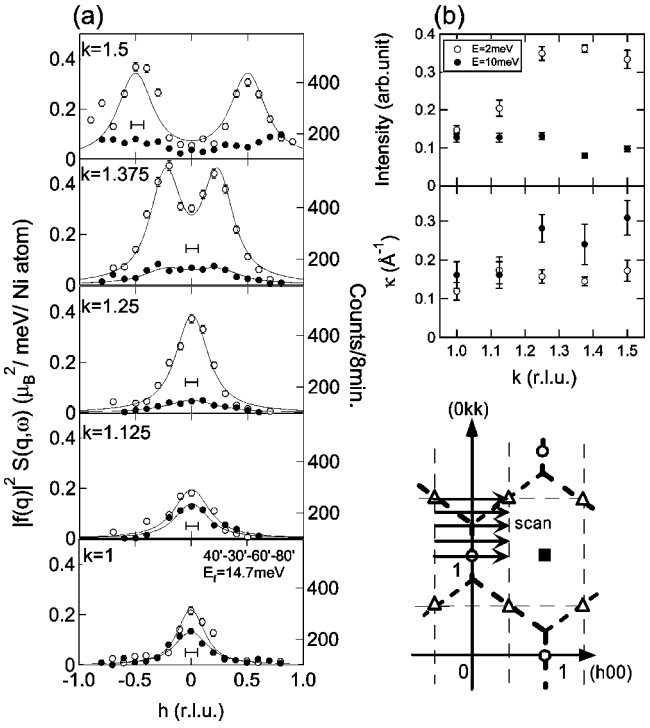


FIG. 8. **Q**-scan spectra at $T=32$ K taken at an energy transfer of 2 meV (open circles) and 10 meV (closed circles). Scans were measured along the [100] direction with (*hkk*) displayed by arrows in the schematic diagram. The absolute value of $S(\mathbf{Q},\omega)$ is shown for reference, obtained by comparison with the intensity of the transverse acoustic phonon. The horizontal bar represents the instrumental resolution width.

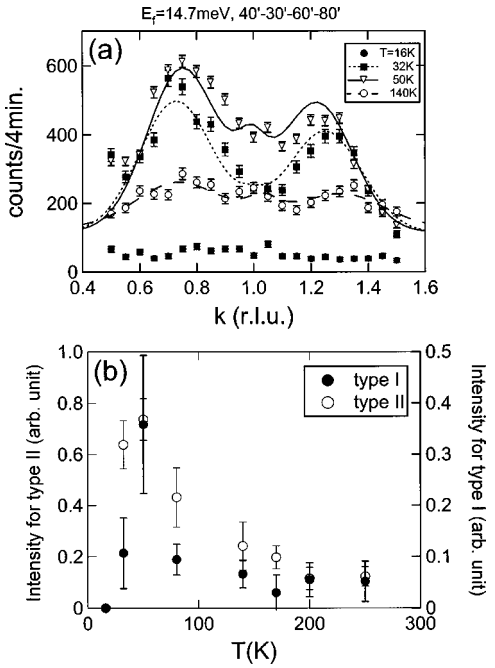


FIG. 9. Temperature dependence of magnetic critical scattering on the fcc Brillouin zone boundary. Scans were performed in constant-energy mode at 2 meV with ($0kk$). Lines in (a) are a fitting of the sum of a Gaussian function for the peak at the fcc zone boundary ($k=0.75$, 1.25) and a Lorentzian function for the peak at the type-I AF Bragg point ($k=1.0$), convolved with the instrumental resolution and magnetic form factor. The thermal variation in integrated intensity of the Lorentzian peak (type-I) and Gaussian peak (type-II) are shown in (b).

energy mode along the [011] direction at the (100) and (300) type-I AF Bragg points with an energy transfer of 2 meV. Symmetric peaks occur at the crossing points of the fcc ZB. The critical scattering appears to be purely magnetic in origin because the **Q** dependence of the three excitations follows the $Ni^{2+}$ form factor.

In order to obtain the entire peak structure for critical scattering at the fcc ZB and inelastic scattering at the type-I AF Bragg point, mesh scans were performed around the (011) with energy transfers of 2 and 10 meV at $T=32$ K, with the results as shown in Fig. 8(a). The mesh scans were measured along the [100] direction with (*hkk*) of $k=1.0$, 1.125, 1.25, 1.375, and 1.5. At 2 meV, broad peaks were observed along the fcc ZB. This data was fitted by Lorentzian functions convolved with the instrumental resolution function. A symmetric peak position and the same peak shape were assumed for the two peaks at $k\geqslant 1.25$. Figure 8(b) is a plot of the peak intensity and $\kappa$ of the Lorentzian peak against the reciprocal index *k*. The intensity for $k=1.375$ and 1.5 represents the data for a single peak. At 2 meV, $\kappa$ is almost constant at 0.15 Å$^{-1}$ across the fcc ZB. However, the critical scattering at the fcc ZB appears to occur in two forms. The peak intensity for $1.25\leqslant k\leqslant 1.5$ is almost flat, and much higher than that for $1\leqslant k<1.25$. The fcc ZB for $1.25\leqslant k\leqslant 1.5$ corresponds to the hexagonal plane, where the type-II AF Bragg points are located at the center, as shown in Fig. 2. Therefore, the critical scattering around

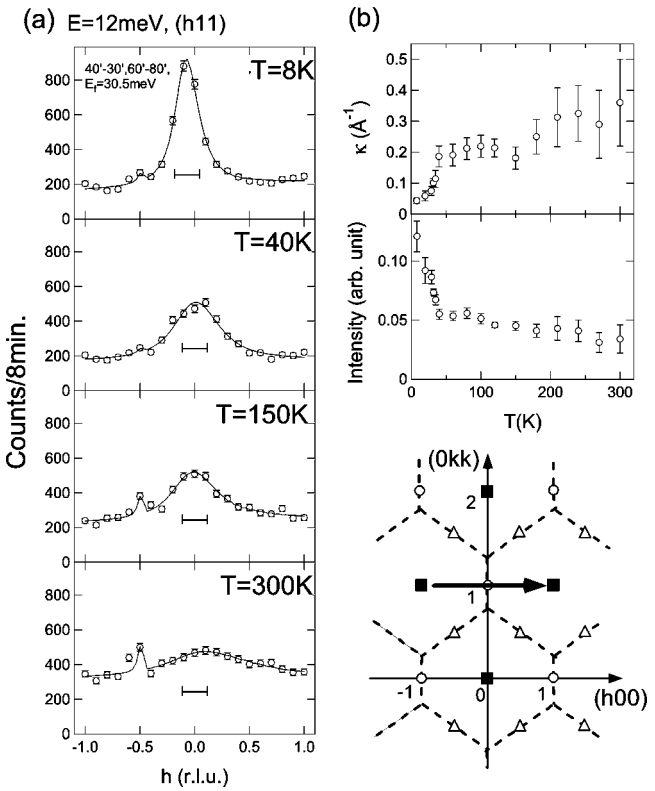


FIG. 10. Temperature dependence of inelastic scattering at the type-I Bragg point with a characteristic energy of 12 meV ($\approx J$). The peak profiles in (a) show **Q** scans at the (011) along the [100] direction as displayed in the schematic diagram. Horizontal bars show the instrumental resolution width. Solid lines are a fitting of three Lorentzian functions for the magnetic peak at the center and phonon peaks at both sides of the magnetic peak, convolved with the instrumental resolution function. (b) Temperature dependence of $\kappa$ and integrated intensity of the magnetic peak.

the type-II Bragg point is considered to extend uniformly to the fcc ZB. Critical scattering in the intermediate phase is contributed to be both type-I and type-II spin fluctuations. The type-I contribution is responsible for magnetic critical scattering extending to the fcc ZB of the rectangular plane, while the type-II contribution produces that for the hexagonal plane, and the AF Bragg points of both points are located at the center (see Fig. 2). At 10 meV, inelastic excitation appears at the type-I AF Bragg point, while the type-II contribution becomes weak and broad.

In the paramagnetic phase, both type-I and type-II contributions are diffusive, as shown in Figs. 5(a) and 6(e). Figure 9 shows the temperature dependence of the type-I and -II contributions. The data was measured in constant-energy mode along the fcc ZB around the (011) with an energy transfer of 2 meV. The fitting lines in Fig. 9(a) were calculated similarly to those in Fig. 6(b). The weak peak at $k=1.0$ and the two strong peaks at $k=0.75$ and 1.25 with $(0kk)$ are associated with the type-I and type-II contributions, respectively. The larger peak at small $k$ is associated with the magnetic form factor. Both type-I and type-II contributions were observed even at 250 K, which is 6 times higher than $T_{N1}$, indicating strong suppression of AF LRO.

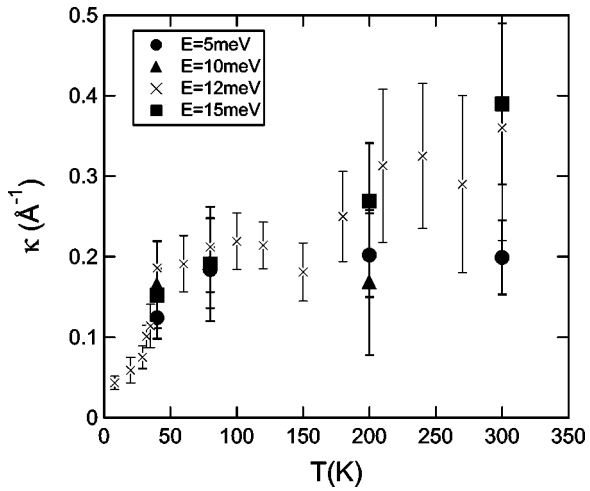


FIG. 11. Temperature dependence of the $\kappa$ of the Lorentzian peak at the type-I AF Bragg point (011), as determined by constant-energy scans along the [100] direction with fixed excitation energy of 5 meV (closed circles), 10 meV (closed triangles), 12 meV (cross marks; the same data as in Fig. 10), and 15 meV (closed squares).

Figure 9(b) shows the temperature dependence of the integrated intensities of the type-I and type-II contributions. The integrated intensities of the critical scattering gradually increase with decreasing temperature from 250 K, and grow rapidly below 150 K, indicating a close correlation between the spin fluctuation and the anomalous behavior of the magnetic and transport properties. Both the type-I and type-II contributions increase towards $T_{N1}$, and are suppressed be-

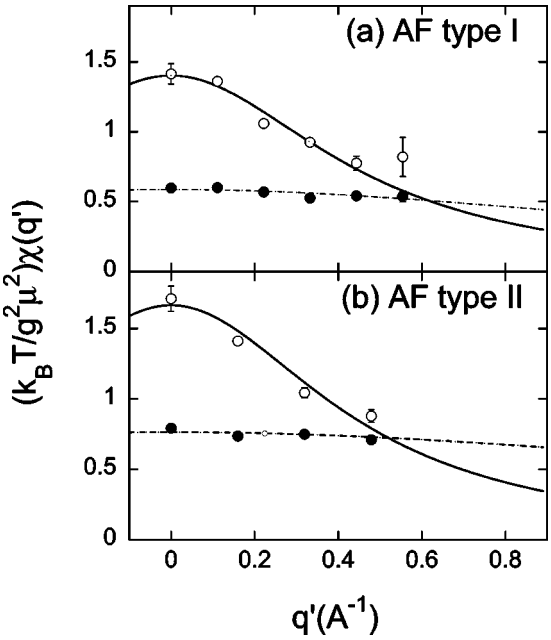


FIG. 12. Wave dependent susceptibility $\chi(q)$ around the (a) type-I and (b) type-II AF Bragg point. The $\mathbf{q}'$ direction is perpendicular to the fcc Brillouin zone boundary at each AF Bragg points. Solid and dashed lines are a fitting of a Lorentzian function convolved with the instrumental resolution function. Horizontal bars show the instrumental resolution width.

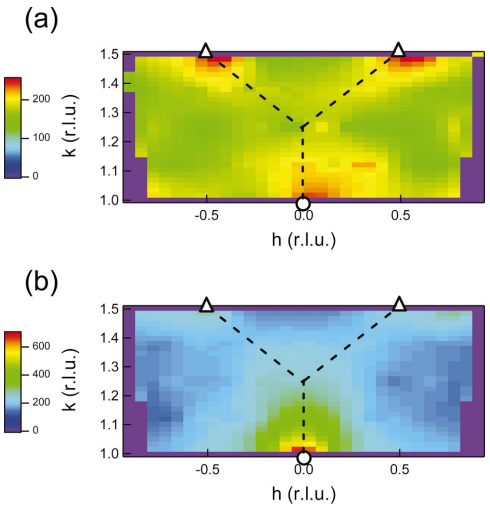


FIG. 13. (Color) Contour maps of magnetic neutron scattering $S(\mathbf{Q},\omega)$ at 11 K with fixed transfer energy of (a) 2 and (b) 13 meV. Data was measured with constant-energy scans over the momentum range $1.0 \leqslant h \leqslant 1.5$ and $-1 \leqslant k \leqslant 1$ with $(hkk)$. Dotted lines display the fcc Brillouin zone boundaries. Open circle and triangles indicate the type-I and type-II AF Bragg points, respectively.

low $T_{N1}$, although these contributions persist into the intermediate phase ($T_{N2} < T < T_{N1}$). The type-I contribution decreases more sharply below $T_{N1}$, associated with the spectral shift of the type-I AF LRO and inelastic scattering above 12 meV. In the low-temperature phase, both type-I and -II contributions disappear, becoming Bragg components for AF LRO, spin waves, and gap excitations above 12 meV. The phase transition at $T_{N2}$ is accompanied by small lattice distortion.[28,29] This small crystal distortion therefore appears to break lattice symmetry and relieve spin frustration.

Figure 10 shows the temperature dependence of the **Q**-scan spectra at the type-I AF Bragg point for a characteristic energy of 12 meV ($\approx J$). The **Q** scans were performed along the [100] direction around the (011). The fitting line is the sum of three Lorentzian functions for the peak at the magnetic zone center (011) and two phonon peaks at $h = \pm 0.5$. The phonon peaks are associated with acoustic branch from nuclear Bragg reflections $(\pm 1,1,1)$. The left phonon peak is sharper than that on the right due to the instrumental resolution. In neutron scattering measurements, the instrumental resolution appears as an ellipse lying in $\mathbf{Q}_\perp$-$\omega$ space (perpendicular to momentum transfer **Q**) with negative slope in the right-handed system. Therefore, the peak for a dispersion surface matching the resolution ellipsoid will be sharpened as a kind of focusing effect. With decreasing temperature, inelastic excitation at 12 meV appears below $T_{N1}$ and grows in parallel with the type-I AF order parameter. In the paramagnetic phase, although the peaks become weak with increasing temperature, magnetic critical scattering exists, even at room temperature (7.5 times $T_{N1}$). This result represents direct confirmations of a short-range correlation in the magnetic susceptibility up to 300 K. The value of $\kappa$ in the range $T_{N1} < T < 150$ K is constant at 0.2 Å$^{-1}$, and increases with temperature above 150 K. Such a saturation of $\kappa$ was also observed at other excitation energies. Figure 11 shows the temperature dependence of $\kappa$ at the type-I AF Bragg point (011). With decreasing temperature from $T = 300$ K, $\kappa$ becomes small, particularly at high energies. Between 150 K and $T_{N1}$, the value of $\kappa$ for all energies converges to 0.2 Å$^{-1}$, indicative of the frustrated nature of the spin system.

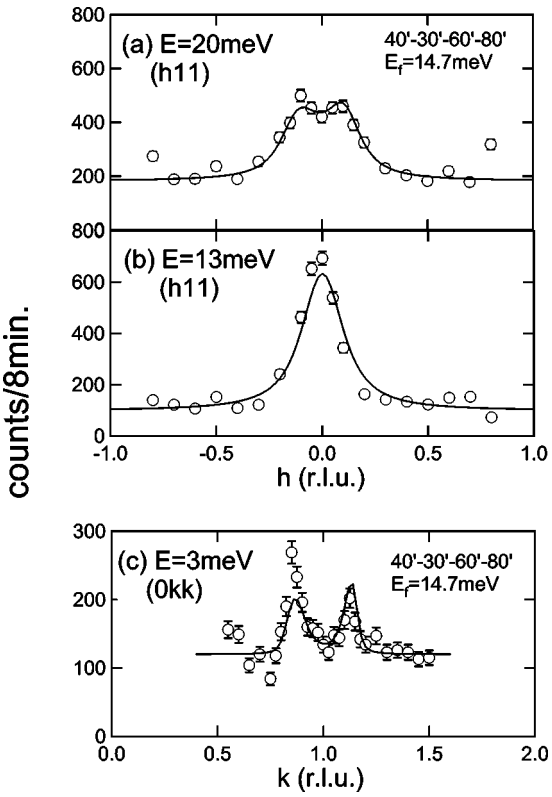


FIG. 14. Peak spectra at the (011) type-I AF Bragg point with an energy transfer of (a) 20 meV, (b) 13 meV, and (c) 3 meV. Measurements were performed at $T = 11$ K along (a), (b) the [100] and (c) [011] directions.

A precise estimation of the correlation length ($\xi$) in the paramagnetic phase was made based on the static momentum dependent magnetic susceptibility $\chi(\mathbf{Q})$ at $T = 100$ and 300 K. Here, $\chi(\mathbf{Q})$ is given by

$$\chi(\mathbf{Q}) = \left(\frac{g^2\mu^2}{k_B T}\right) \int_{-\infty}^{\infty} \left(\frac{1 - e^{-\hbar\omega/k_B T}}{\hbar\omega/k_B T}\right) S(\mathbf{Q},\omega)\, d\omega. \qquad (1)$$

Because the magnetic critical scattering has an intensity of up to $\sim$16 meV, which is much larger than the instrumental resolution width, application of the quasielastic scattering method using a two-axis spectrometer is not sufficient for the present purpose. Therefore, constant-**Q** scans were performed from $-4$ to 16 meV, and $\chi(\mathbf{Q})$ was calculated from the result using Eq. (1). Figure 12 shows $\chi(q')$ at $T = 100$ and 300 K along the [100] direction from (0,1.15,1.15) (type I), and the [111] direction from (1.8,0.65,0.65) (type II). Here, $q'$ represents the distance between a fixed **Q** position and the fcc ZB. At $T = 300$ K, although the magnetic correlations still remain, $\chi(q')$ exhibits a slight $q'$ dependence, giving the $\xi < 0.7$ Å for both type I and type II. At $T = 100$ K, the Lorentzian fitting yields $\xi = 1.9 \pm 0.2$ and 2.1

$\pm 0.2$ Å for type I and type II, respectively. These values correspond to approximately half the distance between the nearest-neighbor atoms. It should be noted that the $\chi(q')$ has the same intensity within experimental error around the both type-I and type-II AF Bragg points in the paramagnetic phase.

In the intermediate and the low-temperature phases, a marked enhancement of the 12-meV gap excitation was observed at the type-I AF Bragg point, as shown in Fig. 10. The **Q** dependence of the gap excitation was studied through constant-energy scans over the momentum region, as shown in the Fig. 8. Figure 13 shows contour maps of magnetic neutron scattering $S(\mathbf{q},\omega)$ at 11 K with a fixed transfer energy of 2 or 13 meV. All the magnetic scattering along the fcc ZB disappears in the low-temperature phase. Magnetic excitations associated with the spin-wave were observed around both the type-I and II AF Bragg points at both 2 and 13 meV. Figure 14 shows peak spectra for the region around the type-I AF Bragg point (011) at $T=11$ K for an energy transfer of 3, 13, and 20 meV. The asymmetric signal is again due to the focusing effect. The gap excitation in Fig. 14(a) splits into two peaks due to a steep dispersion. Fitting two linear dispersion curves at small $q$ for spin gaps of 0 and 12 meV gives slopes of $d\omega/dq=11.2\pm 0.1$ and $59.7 \pm 3.3$ meV Å, respectively.

## V. THEORETICAL ANALYSIS

The antiferromagnet $NiS_2$ exhibits many complicated phenomena, including features similar to frustrated antiferromagnets. These include a structural phase transition, and a non-collinear AF structure at low temperatures. As no unified approach to those phenomena is available as yet, the frustrated magnetism and its relationship with the structural transition are discussed here based on a classical Onsager reaction field approach to a simple Heisenberg picture.

The observed geometrical pattern of critical scattering can be interpreted in part by calculating the momentum-transfer dependence of the energy-integrated scattering law

$$S(\mathbf{Q}) \propto \int d\omega I(\mathbf{Q},\omega)/|F(\mathbf{Q})|^2. \tag{2}$$

Here, $I(\mathbf{Q},\omega)$ and $F(\mathbf{Q})$ are the scattering intensity and magnetic form factor. Under the assumption that the characteristic energy $\hbar\omega$ for the spin fluctuation is smaller than the thermal energy $k_B T$, that is, classical spin fluctuation, Eq. (1) can be approximated as

$$\chi(\mathbf{Q}) \cong \left(\frac{g^2\mu^2}{k_B T}\right) \int_{-\infty}^{\infty} S(\mathbf{Q},\omega) d\omega, \tag{3}$$

which is proportional to the real part $\chi'(\mathbf{Q})$ of the static momentum-dependent magnetic susceptibility via the Kramers-Kronig relation. Consider the classical Heisenberg spin model

$$H_H = -\sum_{\mathbf{Q}} \mathcal{L}(\mathbf{Q}) \hat{S}(\mathbf{Q}) \hat{S}(-\mathbf{Q}), \tag{4}$$

where $\mathcal{L}(\mathbf{Q})$ is the Fourier transform of the exchange interaction matrix. In the classical approximation, the static susceptibility both above and below the Néel temperature $T_{N1}$ can be expressed as

$$\chi(\mathbf{Q}) \sim \{\delta + [1 - \mathcal{L}(\mathbf{Q})/\mathcal{L}(\mathbf{Q}_{\mathrm{AF}})]\}^{-1}, \tag{5}$$

where the parameter $\delta$ specifies the magnitude of deviation of the actual temperature from $T_{N1}$.[39] Here, $\mathbf{Q}_{\mathrm{AF}}$ is the AF wave vector at which the susceptibility diverges when $T = T_{N1}$. Equation (5) is valid, strictly speaking, only when the energy scale of magnetic excitations is much lower than the temperature. At temperatures close to $T_{N1}$, these two quantities are usually comparable. However, since the scattering is mostly quasielastic for all momentum transfers **Q** in the paramagnetic region, this relation can be used to compare the relative intensities at different **Q** points.

Considering the nearest-neighbor (NN) $J_1$, the next-NN $J_2$, and the next-next- (third) NN $J_3$ AF interactions, the Fourier transform of the interaction matrix can be expressed as

$$\mathcal{L}(\mathbf{Q}) = -|J_1|\{\phi_1(\mathbf{Q}) + R_2\phi_2(\mathbf{Q}) + R_3\phi_3(\mathbf{Q})\} \tag{6}$$

in terms of the geometrical factors $\phi_i$ of the fcc lattice

$$\begin{aligned}
\phi_1(\mathbf{Q}) &= 4[\cos(Q_x)\cos(Q_y) + \cos(Q_x)\cos(Q_z) \\
&\quad + \cos(Q_y)\cos(Q_z)], \\
\phi_2(\mathbf{Q}) &= 2[\cos(2Q_x) + \cos(2Q_y) + \cos(2Q_z)], \\
\phi_3(\mathbf{Q}) &= 8[\cos(2Q_x)\cos(Q_y)\cos(Q_z) \\
&\quad + \cos(2Q_y)\cos(Q_x)\cos(Q_z) \\
&\quad + \cos(2Q_z)\cos(Q_x)\cos(Q_y)],
\end{aligned} \tag{7}$$

and the ratios $R_2 = J_2/J_1$ and $R_3 = J_3/J_1$.

Since the value of the AF wave vector depends solely on the parameters $R_2$ and $R_3$, the phase diagram was examined in terms of these coordinates (Fig. 15). The honeycomb structure of the critical scattering in the $(h00)$-$(0kk)$ plane is a *general* feature of fcc lattices with AF interactions up to the third NN. This pattern is robust in a rather large domain, where $R_2 < 0.6$ and $R_3 < 0.3$. Therefore, to locate the position of $NiS_2$ in the phase diagram, it is necessary to study the fine features of the honeycomb structure that are general for the fcc lattice. To fix the values $R_2$ and $R_3$ for $NiS_2$ in the high-symmetry phase, i.e., for $T > T_{N2}$, the critical scattering pattern was calculated for numerous points in phase I. Several points (black rectangles and the circle in Fig. 16) were found to obey the following empirical conditions: the neutron scattering intensity is almost constant along the fcc ZB around type-II Bragg points, and the energy-integrated intensities at the type-I and type-II AF Bragg points are equal within the limit of experimental error. Based on the position of the compound in the phase diagram, $NiS_2$ in a high-symmetry phase appears to be situated in the border separating phases I and II, indicating that the system is nearly frustrated between phases I and II. The possible closeness of the compound to the incommensurate phase is unknown because this phase

was not observed in the experiments, but the experimentally observed coexistence of phases I and II is important to note.

The interatomic magnetic interactions in the type-I AF state were calculated by the LDA+$U$ approach to substantiate the point that frustrated magnetism in $NiS_2$ is driven by the physics of either a Mott-Hubbard or charge-transfer insulator. The effects of on-site Coulomb interaction $U$ on the mean-field level were incorporated into the LDA-based electronic structure.[40] The Coulomb interaction $U$ is essential to obtain the AF solution and the band gap in $NiS_2$. In the insulating state, $U$ gives rise to the well-known superexchange interaction in transition-metal oxides.[41] Another important parameter is the charge-transfer energy $\Delta$, which may also significantly affect the interatomic magnetic interactions in these systems. This energy is sensitive to the relative position of the Ni($3d$) and S($3p$) bands.[42,43] Unfortunately, the LDA+$U$ method, in its present formulation, yields a rather unsatisfactory description for $\Delta$ for transition-metal oxides.[44] Therefore, this effect was modeled by treating both $U$ and $\Delta$ as parameters. In the present definition, $\Delta$ is an additional shift applied to all Ni($3d$) states in the LDA+$U$ calculations. The ratio $U/\Delta$ was chosen to adjust the experimental band gap to $\approx 0.1$ meV.[31] Since the band gap is small, both superexchange and higher-order terms in the $1/U$ expansion (e.g., biquadratic) contribute to the magnetic interactions. Because of this, the magnetic interactions depend not only on the type of fixed magnetic state in which they are calculated, but also on the type of coupling (ferromagnetic or antiferromagnetic) in the atomic pair. The magnetic interactions were averaged over the pairs in the first, second and third coordination spheres. All three attempts gave reasonable positions for $NiS_2$ in the phase diagram (open rectangles in Fig. 15) in the phase-I area, and one of the calculated points is located very close to the place indicated by phenomenological analysis of scattering intensity. The point on the right of the diagram near the line separating the I and II phases requires large charge-transfer energy $\Delta$ ($\Delta = 3$ eV, $U = 4$ eV), whereas the left two points represent smaller values of these parameters ($\Delta = 2$ eV, $U = 5$ eV and $\Delta = 0$ eV, $U = 7.5$ eV, respectively). This circumstance hints at the important role of charge transfer in $NiS_2$.

Since the system is nearly frustrated, suppression of the AF LRO can be expected, and thus the precursors of phase transition should persist to higher temperatures. This means that the critical region is extended considerably. The simplest way to describe this feature is via the Onsager reaction field correction (see the Appendix).[45,46] According to the Onsager approach, the Néel temperature will be notably suppressed when the system is close to the phase border in the phase diagram. Furthermore, at high temperatures, the Onsager approximation converges to the standard Curie-Weiss mean-field result. Therefore, the persistence of precursors of the Néel transition is expected at higher temperatures. Although the Onsager scheme does not provide quantitative agreement with the experimental results, it does account for basic qualitative features observed for $NiS_2$ in the experiments.

Within the framework of the Onsager approach, the effective mean field acting on the ion $i$ spin, as given by $H_i^{\rm eff} = H_i^{\rm ext} + \Sigma_j J_{ij}\langle S_j\rangle$ where $H_i^{\rm ext}$ is an external field, is considered to be overestimated, and a correction of $\Delta H_i^{\rm ef} = -\lambda \Sigma_j J_{ji}\langle S_i\rangle$ is applied. The temperature-dependent parameter $\lambda$ is determined from the sum rule $N^{-1}\Sigma_{\mathbf{q}}^{\rm ZB}\chi'(\mathbf{q}) = S(S+1)/3$, leading to the self-consistent equation

$$T_{N1}^{(0)}/T = N^{-1}\sum_{\mathbf{q}}^{\rm ZB} \mathcal{L}(\mathbf{Q}_l)[\mathcal{L}(0) - \mathcal{L}(\mathbf{q}) + \chi(0)^{-1}]^{-1} \quad (8)$$

from which the uniform static magnetic susceptibility $\chi(0)$ can be determined. The mean-field Curie-Weiss Néel temperature $T_{N1}^{(0)} = \mathcal{L}(\mathbf{Q}_l)S(S+1)/3$ can then be reduced to

$$T_{N1} = T_{N1}^{(0)}/G(1), \quad (9)$$

where

$$G(1) = N^{-1}\sum_{\mathbf{q}}^{\rm ZB} [1 - \mathcal{L}(\mathbf{q})/\mathcal{L}(\mathbf{Q}_l)]^{-1} \quad (10)$$

is the Onsager factor, which depends on lattice structure and dimensionless parameters $R_2$ and $R_3$, i.e., the ratio of exchange interactions in the standard Heisenberg Hamiltonian. Figure 17 illustrates the suppression of the Néel temperature along the line $R_3 = 0.16$ in the phase diagram in Fig. 15. Suppression is most significant near the line separating phases I and II, supporting that the Onsager model qualitatively accounts for the persistence of precursors of the AF transition for nearly frustrated systems.

Evaluation of the temperature dependence of the magnetic characteristics requires the introduction of one additional dimensional parameter $T_{N1}^{(0)}$, which determines in a unique way the renormalized Néel temperature $T_{N1}$ and sets the temperature scale for the persistence of AF transition precursors. In this case, $T_{N1}^{(0)}$ is set to 140 K to account for the experimental value of $T_{N1} = 39.3$ K for the chosen values of $R_2 = 0.43$ and $R_3 = 0.16$. This corresponds to $|J_1| = 84$ K, giving $|\Theta_{\rm CW}| = (12 + 6R_2 + 24R_3)|J_1| \cong 1500$ K, which is in semiquantitative agreement with the experimental value of $|\Theta_{\rm CW}| = 1250$ K mentioned in Sec. II. This agreement also supports the idea that the upper limit of the extended critical region $T \cong 150$ K corresponds to the mean field transition temperature $T_{N1}^{(0)}$. The inset in Fig. 18 demonstrates that the temperature dependence of the uniform magnetic susceptibility deviates from the standard Curie-Weiss behavior. However, the agreement is somewhat qualitative because the theoretical result deviates from the Curie-Weiss law even at $T = 600$ K, whereas the experimentally deviation began at around 350 K. The energy integrated scattering law

$$S(\mathbf{Q}_l) \sim \chi(\mathbf{Q}_l) = [\mathcal{L}(0) - \mathcal{L}(\mathbf{Q}_l) + \chi(0)^{-1}]^{-1} \quad (11)$$

is also shown in Fig. 18 for comparison with the mean-field dependence. As shown in Figs. 17 and 18, the Onsager field correction qualitatively reproduces the experimentally observed persistence of correlation effects at high temperatures in the paramagnetic regime. The Néel temperature is suppressed by the nearly frustrated situation, while the critical scattering intensities of the Curie-Weiss and Onsager approaches coincide at high temperatures.

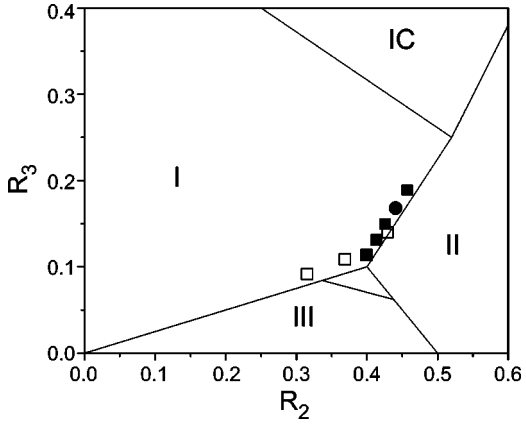


FIG. 15. Magnetic phase diagram for the fcc lattice. Type-I [$\mathbf{Q}_{\mathrm{AF}}=(1,0,0)$], type-II [$\mathbf{Q}_{\mathrm{AF}}=(1/2,1/2,1/2)$], and type-III [$\mathbf{Q}_{\mathrm{AF}}=(1,1/2,0)$] phases are indicated by I, II, and III. The area labeled IC and the small triangle near the crossing of the lines separating the I-II and II-III phases are regions where incommensurate phases may occur. Close rectangles and circle are possible locations of $NiS_2$ in the phase diagram in the high-symmetry phase, as determined by phenomenological analysis of the critical scattering. Open rectangles are the positions of $NiS_2$ in phase diagram according to LDA+$U$ calculations.

The coexistence of type-I and -II AF LRO below $T_{N2}$ cannot be described using the Onsager method because that approach is valid only for the paramagnetic region. Instead, the standard mean-field approximation is employed, and the lattice degrees of freedom are incorporated into the model. The general idea is to explain the coexistence of the type-I and -II AF LRO in terms of the coupling of the magnetic subsystem to the lattice mode $u_{\mathbf{Q}_L}$, which has the appropriate symmetry for mixing the AF LRO. Therefore, if the lattice is distorted ($u_{\mathbf{Q}_L}\neq 0$), coexistence of the two order parameters is possible. Such lattice coupling will have a significant effect only when the two magnetic phases are nearly degenerate and their energies are nearly equal.

To obtain quantitative results, the lattice mode energy $u_{\mathbf{Q}_L}^2/2$ and coupling to the lattice

$$H_c=-\gamma\sum_{\mathbf{q}} u_{\mathbf{Q}_L}\hat{S}(\mathbf{q})\hat{S}(-\mathbf{q}+\mathbf{Q}_L) \tag{12}$$

(mixing modes $\mathbf{Q}_I$ and $\mathbf{Q}_{II}$: $\mathbf{Q}_L=\mathbf{Q}_{II}-\mathbf{Q}_I$) are included in the standard Heisenberg Hamiltonian.

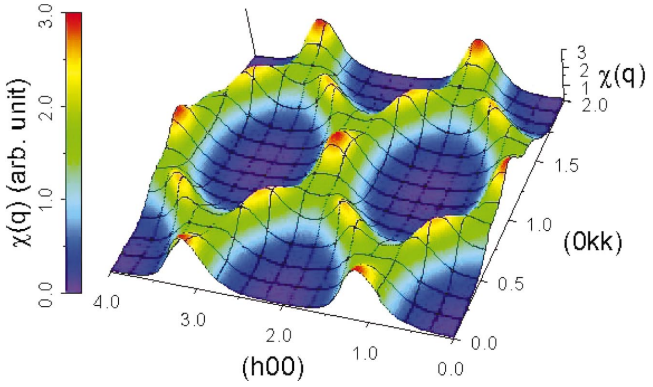


FIG. 16. (Color) Surface of calculated critical scattering intensity for $R_2=0.43$, $R_3=0.16$ (circle in Fig. 15), and $\delta=0.3$.

If it is assumed that the coexistence of order parameters corresponding to the type-I and -II AF LRO is possible, the standard mean-field approximation leads to the following effective Hamiltonian:

$$\begin{aligned}H_{I,II}^{\mathrm{RPA}}=&\mathcal{K}^{\mathrm{eff}}(\mathbf{Q}_I)\sigma_I^2/2+\mathcal{K}^{\mathrm{eff}}(\mathbf{Q}_{II})\sigma_{II}^2/2+u_{\mathbf{Q}_L}^2/2\\&-[\mathcal{K}^{\mathrm{eff}}(\mathbf{Q}_I)\sigma_I+\gamma u_{\mathbf{Q}_L}\sigma_{II}]\hat{S}_z(\mathbf{Q}_I)\\&-[\mathcal{K}^{\mathrm{eff}}(\mathbf{Q}_{II})\sigma_{II}+\gamma u_{\mathbf{Q}_L}\sigma_I]\hat{S}_z(\mathbf{Q}_{II}).\end{aligned} \tag{13}$$

Here, $\sigma_{I,II}$ and $\hat{S}_z(\mathbf{Q}_{I,II})$ are the corresponding magnetizations and spin operators, respectively. The effective values of the interaction matrices can be expressed in terms of fictitious Néel temperatures $T_I^{(0)}=\mathcal{K}^{\mathrm{eff}}(\mathbf{Q}_I)S(S+1)/3$ and $T_{II}^{(0)}=\mathcal{K}^{\mathrm{eff}}(\mathbf{Q}_{II})S(S+1)/3$ at which AF transitions (in the absence of lattice coupling) must occur at the $\mathbf{Q}_I$ and $\mathbf{Q}_{II}$ AF vectors. Here, it is noted that the ratio $\mathcal{K}^{\mathrm{eff}}(\mathbf{Q}_I)/\mathcal{K}^{\mathrm{eff}}(\mathbf{Q}_{II})$ of the *effective constants* of the renormalized mean-field Hamiltonian Eq. (13) does not correspond to the ratio of *bare interactions* $\mathcal{L}(\mathbf{Q}_I)/\mathcal{L}(\mathbf{Q}_{II})=1.05$ evaluated for the parameters used in the Onsager calculations ($R_2=0.34$, $R_3=0.16$, see the circle in Fig. 15). The effective interaction at wave vector $\mathbf{Q}_I$ is increased more by the Onsager reaction field than that at wave vector $\mathbf{Q}_{II}$, with the result that the ratio of effective constants must be considerably larger than that for the bare unrenormalized interactions.

The ground state of the system was found by minimizing the corresponding free energy as follows:

$$\begin{aligned}\mathcal{F}_{I,II}^{\mathrm{RPA}}=&\mathcal{K}^{\mathrm{eff}}(\mathbf{Q}_I)\sigma_I^2/2+\mathcal{K}^{\mathrm{eff}}(\mathbf{Q}_{II})\sigma_{II}^2/2+u_{\mathbf{Q}_L}^2/2\\&-T\ln\left[\sinh\left\{\frac{(2S+1)[\mathcal{K}^{\mathrm{eff}}(\mathbf{Q}_{II})\sigma_{II}+\gamma u_{\mathbf{Q}_L}\sigma_I]}{2T}\right\}\Big/\sinh\left\{\frac{[\mathcal{K}^{\mathrm{eff}}(\mathbf{Q}_{II})\sigma_{II}+\gamma u_{\mathbf{Q}_L}\sigma_I]}{2T}\right\}\right]\\&-T\ln\left[\sinh\left\{\frac{(2S+1)[\mathcal{K}^{\mathrm{eff}}(\mathbf{Q}_I)\sigma_I+\gamma u_{\mathbf{Q}_L}\sigma_{II}]}{2T}\right\}\Big/\sinh\left\{\frac{[\mathcal{K}^{\mathrm{eff}}(\mathbf{Q}_I)\sigma_I+\gamma u_{\mathbf{Q}_L}\sigma_{II}]}{2T}\right\}\right].\end{aligned} \tag{14}$$

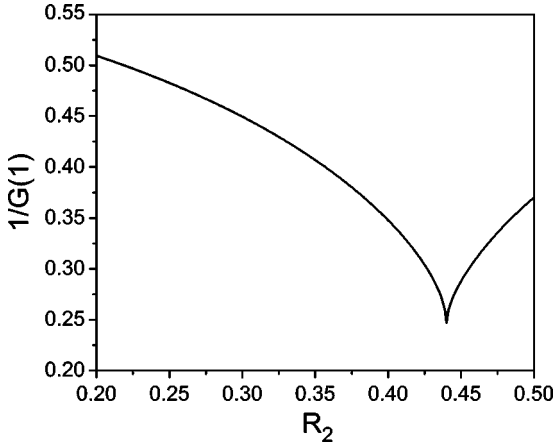


FIG. 17. Dependence of suppression factor $1/G(1)$ for $R_3=0.16$ on $R_2$. The minimum point corresponds to the crossing of the I-II phase boundary.

The intensities of Bragg peaks I and II (Fig. 19) accurately reproduce the experimental situation. The type-I peak arises by a second-order transition, while the type-II reflection arises abruptly at lower temperature accompanied by a structural phase transition (equilibrium $u_{\mathbf{Q}_L}\neq 0$) and a sudden change in the type-I peak intensity. According to the experimentally observed hysteresis, the transition at $T_{N2}$ is first order. The dependence of the free energy on the distortion $u_{\mathbf{Q}_L}$ (and on magnetization $\sigma_{II}$) has two local minima close to $T_{N2}$, the first zero and the second nonzero. Therefore, the change in distortion $u_{\mathbf{Q}_L}$ and magnetization $\sigma_{II}$ is discontinuous, manifesting in a first-order transition. Both reflections coexist at lower temperatures and are compatible with the distorted lattice.

The peculiar features of the compound $NiS_2$ therefore appear to be due to a nearly frustrated situation resulting from closeness to the border separating the type-I and -II AF phases in the phase diagram. The persistence of precursory phases to a higher-temperature critical regime is explained by the nearly frustrated state, and the coexistence of two Bragg reflections at low temperatures is attributed to a structural phase transition that lifts the degeneracy.

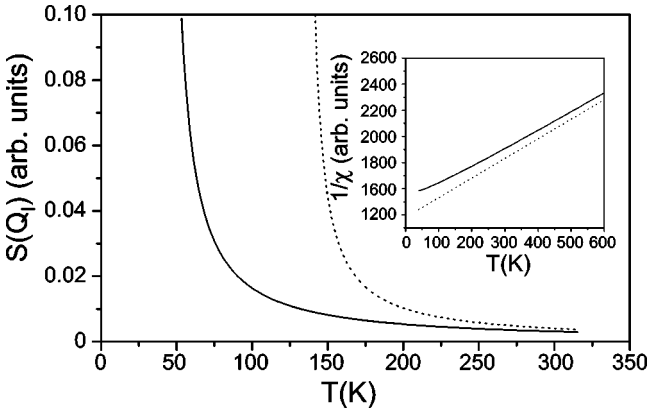


FIG. 18. Temperature dependence of the energy integrated intensity of critical scattering in Curie-Weiss mean-field theory (dotted line) and by the Onsager method (solid line) for $R_3=0.16$ and $R_2=0.43$, corresponding to the circle in Fig. 15. The inset shows the temperature dependence of the inverse uniform magnetic susceptibility in mean-field theory (dashed line) and by the Onsager method (solid line) for the same parameters.

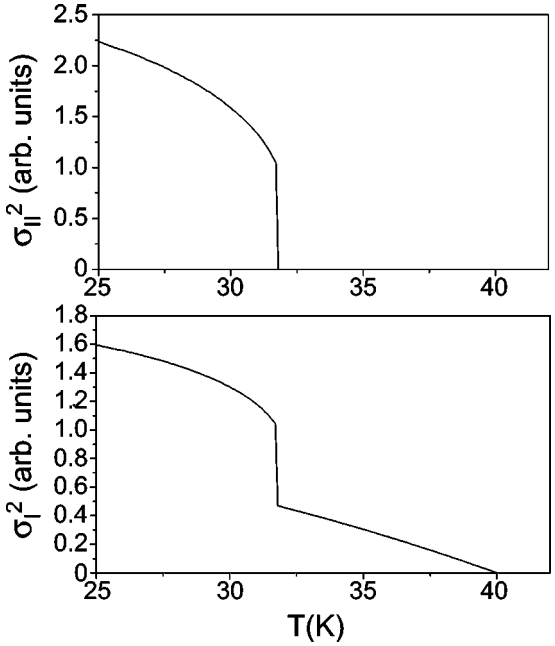


FIG. 19. Temperature dependence of intensity of the type-II (upper) and type-I (lower) Bragg reflections for $\gamma=2.6$, $T_{\mathrm{I}}^{(0)}=40$, $T_{\mathrm{II}}^{(0)}=21$, and $S=1$.

## VI. DISCUSSION

A commonly recognized scenario for frustrated quantum magnets is as follows. The geometrical frustration suppresses the onset of the magnetic LRO, which *enhances* the quantum fluctuation. The degeneracy is then lifted by quantum tunneling between different spin configurations, leading to a unique quantum state with a dominant spin singlet correlation. However, there are several points to be reexamined in this scenario. One is that a simplified model taking into account only the nearest-neighbor exchange interaction is often adopted, in which case the geometrical frustration does not immediately lead to degeneracy of the many spin configurations at the classical level. This is because in real materials, longer range exchange interactions are present, which usually lifts the degeneracy of spin configurations. Another issue is that there are many channels to lift the degeneracy of the classical configuration other than the formation of the quantum spin liquid. One is the order-by-disorder phenomenon.[47] In the classical version, the initial entropy is different for different ground states, and the state with the largest entropy is chosen at finite (even though it is infinitesimal) temperature. The quantum analogue of this order-by-disorder phenomenon is driven by zero-point fluctuation, and the lowest zero-point energy state is chosen. Another channel is coupling to the lattice distortion, which lifts the degeneracy as was found in this study. Therefore, it is necessary to consider the compe-

tition among these different channels to quench entropy at the zero temperature. In this respect, it is misleading to say that frustration *enhances* the quantum fluctuation. The present study on $NiS_2$ found the opposite, in the sense that the frustration enhances the weight of the spin fluctuation at low energies, causing the system to behave more classically compared to the corresponding unfrustrated system (the condition for classical behavior is $\hbar\omega < k_B T$). This criterion supports the validity of the classical approximations to the present frustrated spin systems in the extended critical region between $T_N$ and $T_N^{(0)}$. The degeneracy and accumulation of spectral weight at low energies is lifted by the onset of the LRO and/or coupling to the lattice distortions, which introduces a gap into the spectrum and is accompanied by the appearance of spin-wave dispersion. The inelastic part higher than the gap then behaves quantum mechanically. In this sense, the LRO *enhances* the quantum nature of the spin systems. Based on this observation, the classical spin approximation is adopted here, taking into account the mode-mode coupling through the Onsager reaction field.

First it is instructive to compare the present results for $NiS_2$ with those for the 3D frustrated compound $(Y_{0.97}Sc_{0.03})Mn_2$, which is considered to be capable of a spin liquid state. The parent material, $YMn_2$, is an itinerant antiferromagnet with $T_N \approx 100$ K and a laves phase structure in which Mn tetrahedra form the fcc structure. The compound $(Y_{0.97}Sc_{0.03})Mn_2$ is free of magnetic long range ordering down to the lowest temperature. The magnetic critical scattering observed in $NiS_2$ in the intermediate and paramagnetic phases is reminiscent of $(Y_{0.97}Sc_{0.03})Mn_2$ in the sense that the spectrum exhibits a peak at the fcc ZB. However, these two compounds are critically different in terms of the **Q** dependence. The magnetic scattering in $(Y_{0.97}Sc_{0.03})Mn_2$ appears at the fcc ZB around nuclear Bragg points of (200), (022), and (111), with no signal around the specific reflections of (000), (222), and (400).[33] In contrast, magnetic critical scattering was observed at the fcc ZB around all nuclear Bragg points in $NiS_2$. Figure 20 shows the **Q** dependence of the magnetic critical scattering in the paramagnetic phase. The solid line indicates the magnetic form factor of the $Ni^{2+}$ ion. Both type-I and type-II contributions follow the magnetic form factor except at (011), where it is though that the deviation at (011) is supposed that the neutron scattering observations are in fact visualizing perpendicular components ($S_\perp$) of spin fluctuation with respect to the scattering vector. If a noncollinear type-I AF spin lattice is assumed,[24,25] $S_\perp$ at (011) is half that at (100). Therefore, the magnetic critical scattering in $NiS_2$ has no structure factor in the paramagnetic phase, and its geometrical pattern is determined only by the ratios of the exchange interspin interactions $R_2$ and $R_3$.

The absence of a signal at the fcc ZB around specific Bragg points in $(Y_{0.97}Sc_{0.03})Mn_2$ is the consequence of strong spin singlet formation within the Mn tetrahedra, which promotes the contribution of the structure factor to the **Q** dependence of magnetic critical scattering intensity, as has been proved for the spin liquid state.[48,49] In other words, the peculiar features of critical scattering in $(Y_{0.97}Sc_{0.03})Mn_2$ are due to quantum fluctuations around a singlet ground state

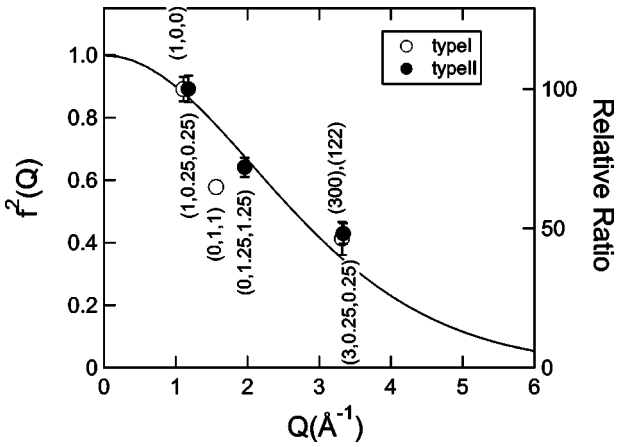


FIG. 20. Wave-vector dependence of the intensity of critical scattering. The solid line represents the magnetic form factor of the $Ni^{2+}$ ion as a function of magnitude of the wave vector **Q**. Open and closed circles indicate the integrated intensity of the type-I ($T = 80$ K) and type-II ($T = 32$ K) contributions. The intensity is normalized to 100 at (100) for the type-I contribution and to 88 at (1,0.25,0.25) for the type-II contribution.

with long-range correlations. On the other hand, the ground state of $NiS_2$ is ordered AF with classical spin fluctuations that are restricted to short-range distances. This is consistent with the much shorter correlation length $\approx 2$ Å at 100 K, which reaches only to nearest neighbors and is much smaller than the size of the elementary cell containing four $Ni^{2+}$ ions.

Analysis of the frustrated situation in $NiS_2$ reveals the crucial influence of the scale and strength of the exchange inter-spin interactions on the degree of frustration. The ratio of $T_N$ to $T_{CW}$ is a good measure for frustration. For $NiS_2$, $T_N/T_{CW} = 30$, which is equal to or larger than that in other frustrated systems; 16 for $LiCrO_2$ (triangular),[50] and 24 for $ZnCr_2O_4$ (spinel).[51] This indicates that the geometry of the lattice is not solely responsible for the properties of strongly frustrated magnets. It is known that a 3D fcc lattice with AF NN interactions is highly frustrated, as indicated by the infinite number of zero-energy modes situated along the manifold of lines in 3D momentum space $[(\pm\pi, Q_y, 0)$, $(Q_y, \pm\pi, 0)$, etc.] in the spectrum derived from the mean-field description. However, the next NN interactions destroy this highly frustrated picture and the system becomes accidentally frustrated between different AF LRO (see the phase diagram in Fig. 15) only for specific values of interaction parameters. Even in the case of accidental frustration, the degree of frustration will be considerably smaller because the measure of zero-energy modes is zero-dimensional (points), not one-dimensional (lines). For example, in the border between phases I and II, zero-energy modes are located at wave vectors corresponding to AF vectors of type-I and type-II. The same considerations apply to triangular, *kagomé*, and other lattices, which are considered as plausible candidates for frustration phenomena based solely on the type of crystal lattice and the *assumption* of the exclusive role of NN spin-spin interaction. The next-NN interactions can destroy the geometrical arguments in these lattices in a similar way as

observed for the fcc crystal structure. Based on the above considerations, it can be concluded that no actual system is ever ''completely frustrated'' but is always ''nearly frustrated'' depending on the pattern of interactions in a given geometrical structure of a spin system. Even ''nearly frustrated'' situations give rise to significant violations of the properties known from Curie-Weiss treatment, as observed experimentally for $NiS_2$ and as revealed theoretically through a simple Onsager reaction field approach.

In the present experiments, two crossovers were observed in the paramagnetic phase of $NiS_2$. One is from the paramagnetic state to a short-ranged AF state at higher temperature. We found that the uniform magnetic susceptibility starts to deviate from the Curie-Weiss law at $\approx 350$ K, and magnetic critical scattering at the type-I AF Bragg point was observed at least up to room temperature. Therefore, the short-range AF correlation is considered to begin to grow below this crossover temperature. The other crossover corresponds to the rapid enhancement of low-energy excitation extending to the fcc ZB at $\approx 150$ K. In addition, spin-glass behavior, and metallic transport were observed below 150 K. However, these crossovers are partially attributable to a change in surface magnetism and transport. Thio *et al.*[32] observed that the transport properties in $NiS_2$ are dominated by surface conduction below 150 K. The spin-glass signal was confirmed in the present study to depend on the surface-area to volume ratio. Although the spin-glass and metallic behavior include a surface contribution, these anomalies should correlate closely with the bulk property, particularly geometrical spin frustration.

We observed that the diffusive spectra at both the type-I and -II AF Bragg points shift to a finite energy in the AF LRO phase. Such a spectral shift has also been observed in other frustrated compounds, for example, $CuGeO_3$ or the spinel compound $ZnCr_2O_4$. These phase transitions are accompanied by a lattice distortion that removes the degeneracy of ground states. However, this is not the case for $NiS_2$ because the spectral shift occurs at $T_{N1}$ at which no lattice distortion was observed. The integrated intensity of 12-meV excitation reveals the same temperature dependence as the type-I AF LRO, as shown in Fig. 10. Since the spin lattice of the type-I AF LRO in $NiS_2$ contains four sublattices, it is suggested that the high-energy excitation may be an optical mode of the spin-wave excitation.

In conclusion, we have studied the spin dynamics in $NiS_2$ and revealed the effects of frustration. The characteristic features of macroscopic magnetism of frustrated magnets were observed, such as hysteresis in the magnetization processes and suppression of AF LRO. Neutron scattering experiments revealed a honeycomb pattern of magnetic critical scattering in reciprocal lattice space (continuous-line structure along the fcc Brillouin zone boundaries), providing direct evidence for nearly frustrated AF on the fcc lattice. From theoretical analysis, it was concluded that the system is located very close to the phase boundary between the type-I and II AF phases, leading to the observed extended critical spin fluctuation along the fcc ZB and hence classical behavior. The onset of the AF LRO and/or lattice distortion produces spin-wave dispersion and gap excitation, lifting the degeneracy. In this sense, the quantum nature of the spin is recovered by the AF LRO. This observation leads to a number of possible prescriptions for how to search for the quantum spin liquid state. One is to minimize the spin quantum number to the lowest $S=1/2$. Another is to reduce the coupling to the lattice distortion, and yet another is to eliminate the order-by-disorder phenomenon. It is well known that the pyrochlore lattice does not exhibit the classical order-by-disorder phenomenon, whereas the *kagomé* lattice does.[52] However it is rather difficult to avoid the quantum order-by-disorder phenomenon, and the only way to resolve the situation seems to be again to reduce the spin quantum number *S*. It is not clear whether a larger volume or measurement of the degeneracy in momentum space will be better for a quantum spin liquid, which is left for future study.

## ACKNOWLEDGMENTS

The authors acknowledge S. Maekawa and W. Koshibae for fruitful discussions and K. Hirota for assistance in neutron scattering measurements. M.M. was supported by the Japan Society for the Promotion of Science for Young Scientists. N.N. was supported by Priority Areas Grants and a Grant-in-Aid for COE research from the Ministry of Education, Science, Culture and Sports of Japan. A.S.M. acknowledges RFBR Grant No. 01-02-16508. Y.E. was also supported by a Grant-in-Aid for Scientific Research sponsored by JSPS.

## APPENDIX: ONSAGER'S REACTION FIELD

In this Appendix, we describe the Onsager's reaction field and derive Eqs. (8)–(11) for the self-consistent procedure. We begin with the Heisenberg spin Hamiltonian

$$H=-\frac{1}{2}\sum_{ij} J_{ij}\vec{S}_i\cdot\vec{S}_j-\sum_i H_i^{\mathrm{ext}}S_i^z$$

$$=-\sum_{\mathbf{Q}} \mathcal{L}(\mathbf{Q})\hat{S}_{\mathbf{Q}}\cdot\hat{S}_{-\mathbf{Q}}-\sum_{\mathbf{Q}} H_{\mathbf{Q}}^{\mathrm{ext}}, \tag{A1}$$

where

$$\mathcal{L}(\mathbf{Q})=\frac{1}{2}\sum_{ij} J_{ij}e^{i\mathbf{Q}\cdot(\vec{R}_i-\vec{R}_j)}. \tag{A2}$$

Using the usual mean field treatment, we decouple the spin-spin interaction

$$\vec{S}_i\cdot\vec{S}_j\rightarrow\langle\vec{S}_i\rangle\cdot\vec{S}_j+\vec{S}_i\cdot\langle\vec{S}_j\rangle-\langle\vec{S}_i\rangle\cdot\langle\vec{S}_j\rangle \tag{A3}$$

which results in the molecular field approximation

$$H_i^{\mathrm{MF}}=H_i^{\mathrm{ext}}+\sum_j J_{ij}\langle S_j^z\rangle \tag{A4}$$

applied to the $z$ component of the spin $\vec{S}_i$. What Onsager pointed out is that $H_i^{\mathrm{MF}}$ includes some overcounting, which

should be subtracted. This part of the effective field $H_i^{\rm reaction}$ is called the reaction field, and is given by

$$\chi_{ii}H_i^{\rm reaction}=\sum_{ij}\ \chi_{ij}H_{i\to j}^{\rm MF}=\sum_{ij}\ \chi_{ij}J_{ji}\langle S_i^z\rangle, \tag{A5}$$

where $\chi_{ij}$ is the static magnetic susceptibility between sites $i$ and $j$. For classical spins, $\chi_{ij}$ is given by

$$\chi_{ij}=\langle S_i^z S_j^z\rangle/T, \tag{A6}$$

where $T$ is the temperature ($k_B=1$), and especially $\chi_{ii}=\langle (S_i^z)^2\rangle=\chi_0=S(S+1)/(3T)$. The physical meaning of this reaction field follows. $\langle S_i^z\rangle$ creates the effective field $H_{i\to j}^{\rm MF}=J_{ji}\langle Sz_i\rangle$ at site $j$, which induces the magnetization $\chi_{ij}H_{i\to j}^{\rm MF}$ at site $i$. This effect should not be taken into account and subtracted from the expectation value $\langle S_i^z\rangle$. Therefore, the reaction field $H_i^{\rm reaction}$ should be subtracted from $H_i^{\rm MF}$, and the effective field $H_i^{\rm eff}$ applied to the spin $S_i^z$ is

$$\begin{aligned}H_i^{\rm eff}&=H_i^{\rm MF}-H_i^{\rm reaction}\\&=H_i^{\rm ext}+\sum_j\ J_{ij}\langle S_j^z\rangle-\sum_j\ \lambda_{ij}J_{ji}\langle S_i^z\rangle,\end{aligned} \tag{A7}$$

where $\lambda_{ij}=\chi_{ij}/\chi_0$. In terms of this effective field, the Fourier component of $\langle S_i^z\rangle$ is given by

$$\langle S_{\mathbf{Q}}^z\rangle=\chi_0 H_{\mathbf{Q}}^{\rm eff}=\chi_0[H_{\mathbf{Q}}^{\rm ext}+\mathcal{L}(\mathbf{Q})\langle S_{\mathbf{Q}}^z\rangle-\lambda\langle S_{\mathbf{Q}}^z\rangle], \tag{A8}$$

where

$$\lambda=\frac{1}{N}\sum_{ij}\ \lambda_{ij}J_{ji}=\frac{1}{\chi_0}\frac{1}{N}\sum_{\mathbf{Q}}\ \chi(\mathbf{Q})\mathcal{L}(\mathbf{Q}). \tag{A9}$$

Then the static susceptibility $\chi(\mathbf{Q})$ is given as

$$\chi(\mathbf{Q})=\langle S_{\mathbf{Q}}^z\rangle/H_{\mathbf{Q}}^{\rm ext}=\frac{\chi_0}{1-\chi_0[\mathcal{L}(\mathbf{Q})-\lambda]}. \tag{A10}$$

Obtaining $\lambda$ at $\mathbf{Q}=0$,

$$\lambda=\chi(0)^{-1}-\chi_0^{-1}+\mathcal{L}(0) \tag{A11}$$

which is Eq. (11). Putting Eq. (A10) into Eq. (A9), we obtain the self-consistent equation for $\lambda$:

$$\lambda=\frac{1}{\chi_0}\frac{1}{N}\sum_{\mathbf{Q}}\ =\frac{\chi_0\mathcal{L}(\mathbf{Q})}{1-\chi_0[\mathcal{L}(\mathbf{Q})-\lambda]}. \tag{A12}$$

This equation can be transformed easily into

$$1=\frac{1}{N}\sum_{\mathbf{Q}}\ \frac{1}{1-\chi_0[\mathcal{L}(\mathbf{Q})-\lambda]}. \tag{A13}$$

Now let us assume that $\mathcal{L}(\mathbf{Q})$ has the maximum at $\mathbf{Q}=\mathbf{Q}$, and define the mean field transition temperature $T_0$ by

$$\chi_0(T_0)\mathcal{L}(\mathbf{Q})=1, \tag{A14}$$

which leads to $T_0=S(S+1)\mathcal{L}(\mathbf{Q})/3$. Then Eq. (A13) can be further transformed into

$$\frac{T_0}{T}=G[\lambda/\mathcal{L}(\mathbf{Q})+T/T_0], \tag{A15}$$

where the function $G(s)$ is given by

$$G(s)=\frac{1}{N}\sum_{\mathbf{Q}}\ \frac{1}{s-\mathcal{L}(\mathbf{Q})/\mathcal{L}(\mathbf{Q})}. \tag{A16}$$

The transition temperature is signaled by the divergence of $\chi(\mathbf{Q})$, namely, the condition $1-\chi_0[\mathcal{L}(\mathbf{Q})-\lambda]=0$. This condition is equivalent to that the argument of $G$ in Eq. (A15), i.e., $\lambda/\mathcal{L}(\mathbf{Q})+T/T_0$, is equal to 1. Therefore, the transition temperature $T_c$ is determined by

$$\frac{T_0}{T_c}=G(1). \tag{A17}$$

Equation (8) can be obtained from Eq. (A13) using the definition of $\lambda$ (A11).

*Electronic address: matsuuram@ornl.gov; Present address: Solid State Division, Oak Ridge National Laboratory, Oak Ridge, Tennessee 37831-6430, USA.

†Present address: International Institute for Advanced Studies, Kizu, Kyoto 619-0225, Japan.

‡Present address: Institute for Materials Research, Tohoku University, Aoba-ku, Sendai 980-8577, Japan.

[1] A.P. Ramirez, Annu. Rev. Mater. Sci. **24**, 453 (1994).

[2] A.P. Ramirez, G.O. Espinosa, and A.S. Cooper, Phys. Rev. Lett. **64**, 2070 (1990).

[3] I.S.H.Q. Huang, X.P.A. Gao, A.P. Ramirez, and R.J. Cava, Phys. Rev. Lett. **86**, 894 (2001).

[4] J.E. Greedan, J.N. Reimers, C.V. Stager, and S.L. Penny, Phys. Rev. B **43**, 5682 (1991).

[5] J.N. Reimers, J.E. Greedan, C.V. Stager, M. Bjorgvinnsen, and M.A. Subramanian, Phys. Rev. B **43**, 5692 (1991).

[6] M.J. Harris, M.P. Zinkin, and T. Zeiske, Phys. Rev. B **56**, 11 786 (1997).

[7] J.S. Gardner *et al.*, Phys. Rev. Lett. **82**, 1012 (1999).

[8] J.E. Greedan, N.P. Raju, A.S. Wills, C. Morin, and S.M. Shaw, Chem. Mater. **10**, 3058 (1998).

[9] A.S. Wills, N.P. Raju, and J.E. Greedan, Chem. Mater. **11**, 1510 (1999).

[10] M.J.P. Gingras, C.V. Stager, N.P. Raju, B.D. Gaulin, and J.E. Greedan, Phys. Rev. Lett. **78**, 947 (1997).

[11] C.H. Booth, J.S. Gardner, G.H. Kwei, R.H. Heffner, F. Bridges, and M.A. Subramanian, Phys. Rev. B **62**, R755 (2000).

[12] S.-H. Lee, C. Broholm, T.H. Kim, W. Ratcliff II, and S.-W.

Cheong, Phys. Rev. Lett. **84**, 3718 (2000).
[13] N.C. Tombs and H.P. Rooksby, Nature (London) **165**, 442 (1950).
[14] J.M. Hastings and L.M. Corliss, Phys. Rev. B **14**, 1995 (1976).
[15] C.A. Bailey and P.L. Smith, Phys. Rev. **114**, 1010 (1959).
[16] M.S. Lin and H. Hacker, Jr., Solid State Commun. **6**, 687 (1968).
[17] J.M. Hastings, N. Elliott, and L.M. Corliss, Phys. Rev. **115**, 13 (1959).
[18] J.M. Hastings and L.M. Corliss, IBM J. Res. Dev. **14**, 227 (1970).
[19] T. Miyadai, K. Takizawa, H. Nagata, H. Ito, S. Miyahara, and K. Hirakawa, J. Phys. Soc. Jpn. **38**, 115 (1975).
[20] K. Yoshida and S. Inagaki, J. Phys. Soc. Jpn. **50**, 3268 (1981).
[21] K. Yoshida and S. Inagaki, J. Phys. Soc. Jpn. **50**, 769 (1981).
[22] J.A. Wilson, *The Metallic and Non-metallic States of Matter* (Taylor & Francis, London, 1985), Chap. 9.
[23] A. Fujimori, K. Mamiya, T. Mizokawa, T. Miyadai, T. Sekiguchi, H. Takahashi, N. Môri, and S. Suga, Phys. Rev. B **54**, 16 329 (1996).
[24] K. Kikuchi, T. Miyadai, T. Fukui, H. Itô, and K. Takizawa, J. Phys. Soc. Jpn. **44**, 410 (1978).
[25] K. Kikuchi, T. Miyadai, H. Ito, and T. Fukui, J. Phys. Soc. Jpn. **45**, 444 (1978).
[26] Y. Nishihara, S. Ogawa, and S. Waki, J. Phys. Soc. Jpn. **39**, 63 (1975).
[27] K. Kikuchi, J. Phys. Soc. Jpn. **47**, 484 (1979).
[28] H. Nagata, H. Ito, and T. Miyadai, J. Phys. Soc. Jpn. **41**, 2133 (1976).
[29] T. Thio, J.W. Bennett, and T.R. Thurston, Phys. Rev. B **52**, 3555 (1995).
[30] R. Shindou and N. Nagaosa, Phys. Rev. Lett. **87**, 116801 (2001).
[31] M. Matsuura, H. Hiraka, K. Yamada, and Y. Endoh, J. Phys. Soc. Jpn. **69**, 1503 (2000).
[32] T. Thio and J.W. Bennett, Phys. Rev. B **50**, 10 574 (1994).
[33] R. Ballou, E. Leliévre-Berna, and B. Fåk, Phys. Rev. Lett. **76**, 2125 (1996).
[34] S. Sudo and T. Miyadai, J. Phys. Soc. Jpn. **54**, 3934 (1985).
[35] X. Yao, Y.-K. Kuo, D.K. Powell, J.W. Brill, and J.M. Honig, Phys. Rev. B **56**, 7129 (1997).
[36] P. Kwizera, M.S. Dresselhaus, and D. Adler, Phys. Rev. B **21**, 2328 (1980).
[37] S. Ogawa, J. Phys. Soc. Jpn. **41**, 462 (1976).
[38] K. Adachi, K. Sato, K. Yamaguchi, and M. Ohashi, J. Phys. Soc. Jpn. **32**, 573 (1972).
[39] W. Marshall and S.W. Lovesay, *Theory of Thermal Neutron Scattering* (Oxford University Press, Oxford, 1971).
[40] Notice, that LDA (local-density approximation) is based on the homogeneous electron gas picture for exchange and correlations.
[41] P.W. Anderson, Phys. Rev. **115**, 2 (1959).
[42] T. Oguchi, K. Terakura, and A.R. Williams, Phys. Rev. B **28**, 6443 (1983).
[43] J. Zaanen and G.A. Sawatzky, Can. J. Phys. **65**, 1262 (1987).
[44] I.V. Solovyev and K. Terakura, Phys. Rev. B **58**, 15 496 (1998).
[45] R.M. White, *Quantum Theory of Magnetism* (Springer-Verlag, New York, 1983).
[46] Onsager field correction was previously applied for ferromagnets and we are not aware of an attempt to describe behavior of frustrated magnets within this approach.
[47] J. Villain, Z. Phys. B: Condens. Matter **33**, 31 (1979).
[48] A.S. Mishchenko, Pis'ma Zh. Eksp. Teor. Fiz. **68**, 480 (1998) [JETP Lett. **68**, 514 (1998)].
[49] Y. Kagan, K.A. Kikoin, and A.S. Mishchenko, Phys. Rev. B **55**, 12 348 (1997).
[50] A. Tauber, W.M. Moller, and E. Banks, J. Solid State Chem. **4**, 138 (1985).
[51] P.K. Baltzer, P.J. Wojtowicz, M. Robbins, and E. Lopatin, Phys. Rev. **151**, 367 (1966).
[52] R. Moessner and J.T. Chalker, Phys. Rev. Lett. **80**, 2929 (1998).